MNRAS **000**, 1–21 (0000) Preprint 7 August 2018 Compiled using MNRAS LATEX style file v3.0

The structure of post-starburst galaxies at $0.5 < z < 2$: evidence for two distinct quenching routes at different epochs

David T. Maltby,[1]★ Omar Almaini,[1] Vivienne Wild,[2] Nina A. Hatch,[1]
William G. Hartley,[3] Chris Simpson,[4] Kate Rowlands[5] and Miguel Socolovsky[1]
[1]*School of Physics and Astronomy, University of Nottingham, University Park, Nottingham NG7 2RD, UK*
[2]*School of Physics and Astronomy, University of St Andrews, North Haugh, St Andrews KY16 9SS, UK*
[3]*Department of Physics and Astronomy, University College London, 3rd Floor, 132 Hampstead Road, London NW1 2PS, UK*
[4]*Gemini Observatory, Northern Operations Center, 670 N. A'ohoku Place, Hilo, HI 96720, USA*
[5]*Department of Physics and Astronomy, Johns Hopkins University, Bloomberg Center, 3400 N. Charles St., Baltimore, MD 21218, USA*

Accepted 2018 June 28. Received 2018 June 07; in original form 2017 December 07

ABSTRACT

We present an analysis of the structure of post-starburst (PSB) galaxies in the redshift range $0.5 < z < 2$, using a photometrically-selected sample identified in the Ultra Deep Survey (UDS) field. We examine the structure of ~ 80 of these transient galaxies using radial light $\mu(r)$ profiles obtained from CANDELS *Hubble Space Telescope* near-infrared/optical imaging, and compare to a large sample of ~ 2000 passive and star-forming galaxies. For each population, we determine their typical structural properties (effective radius r_e, Sérsic index n) and find significant differences in PSB structure at different epochs. At high redshift ($z > 1$), PSBs are typically massive ($M_* > 10^{10}\,M_\odot$), very compact and exhibit high Sérsic indices, with structures that differ significantly from their star-forming progenitors but are similar to massive passive galaxies. In contrast, at lower redshift ($0.5 < z < 1$), PSBs are generally of low mass ($M_* < 10^{10}\,M_\odot$) and exhibit compact but less concentrated profiles (i.e. lower Sérsic indices), with structures similar to low-mass passive discs. Furthermore, for both epochs we find remarkably consistent PSB structure across the optical/near-infrared wavebands (which largely trace different stellar populations), suggesting that any preceding starburst and/or quenching in PSBs was not strongly centralized. Taken together, these results imply that PSBs at $z > 1$ have been recently quenched during a major disruptive event (e.g. merger or protogalactic collapse) which formed a compact remnant, while at $z < 1$ an alternative less disruptive process is primarily responsible. Our results suggest that high-z PSBs are an intrinsically different population to those at lower redshifts, and indicate different quenching routes are active at different epochs.

Key words: galaxies: evolution — galaxies: fundamental parameters — galaxies: high-redshift — galaxies: structure

1 INTRODUCTION

In the local Universe, a strong bimodality is observed in several galaxy properties, e.g. optical colour, morphology and spectral-type (e.g. Strateva et al. 2001). In general, massive galaxies tend to be red, passive and of early-type morphology (i.e. elliptical, S0), while lower mass galaxies tend to be blue, star-forming and of late-type morphology (i.e. spiral). These two populations are now commonly called the *red-sequence* and the *blue cloud*, respectively. In recent years, large-scale photometric surveys have enabled the evolution of this bimodality and the formation/build-up of the red-sequence to be traced out to $z > 2$ (e.g. Bell et al. 2004; Cirasuolo et al. 2007; Faber et al. 2007; Brammer et al. 2011; Muzzin et al. 2013). However, despite significant progress, we still do not fully understand how star formation is quenched at high redshift, as required to transfer galaxies from the blue cloud on to the red-sequence.

Although the principal drivers for quenching star formation in galaxies remain uncertain, various physical mechanisms have been proposed. For example, the stripping of the interstellar medium (e.g. Gunn & Gott 1972), gas-removal by AGN or starburst-driven superwinds (e.g. Silk & Rees 1998; Hopkins et al. 2005; Diamond-Stanic et al. 2012), or an exhaustion of the gas supply via strangulation (e.g. Larson et al. 1980). Other possible processes include morphological quenching (e.g. Martig et al. 2009), and the shock heating of infalling cold gas by the hot halo (e.g. Dekel & Birnboim 2006). Furthermore, in addition to these 'initial' quenching processes, radio-mode AGN feedback may also be required to prevent further gas accretion and keep star formation suppressed on longer timescales (Best et al. 2005, 2006).

For massive galaxies, the quenching of star formation is also accompanied by a significant evolution in their structural properties. Massive galaxies at high redshift ($z \sim 2$) are typically disc-dominated, while in the local Universe they are generally spheroidal (e.g. van der Wel et al. 2011; Buitrago et al. 2013). This struc-

★ E-mail: david.maltby@nottingham.ac.uk

© 0000 The Authors

tural transition appears to occur at $z > 1$ for most galaxies with $M_* > 10^{10.5}\,M_\odot$ (Mortlock et al. 2013). However, it is currently unclear whether this transition occurs during the same event that quenched the star formation. In addition, massive passive galaxies in the early Universe also appear to be significantly more compact than their local counterparts (e.g. Trujillo et al. 2006). This implies a dramatic size growth via e.g. minor mergers (Naab et al. 2009), although other scenarios are possible (e.g. progenitor bias; Carollo et al. 2013). Possible mechanisms for the formation of these compact high-z galaxies (i.e. *red nuggets*) include: i) central starbursts triggered by either a gas-rich merger (Hopkins et al. 2009; Wellons et al. 2015) or dissipative 'protogalactic collapse' (Dekel et al. 2009; Zolotov et al. 2015), which is followed by a rapid quenching through e.g. AGN or starburst-driven superwinds (e.g. Hopkins et al. 2005); and ii) a formation at very early times when the Universe itself was much denser (Wellons et al. 2015).

To identify the processes driving quenching and structural evolution at high redshift, it is useful to consider galaxies that have been recently quenched (i.e. caught in transition). The rare class of post-starburst (PSB) galaxies is one such example, as they represent systems in which a major burst of star formation was rapidly quenched within the last few hundred Myr. Spectroscopically, these galaxies are identified from the characteristic strong Balmer absorption lines related to an enhanced A-star population, combined with a general lack of strong emission lines (Dressler & Gunn 1983; Wild et al. 2009). However, due to their intrinsic short-lived nature, until recently only a handful of these rare galaxies had been spectroscopically identified at $z > 1$ (e.g. Vergani et al. 2010; Bezanson et al. 2013; van de Sande et al. 2013; Newman et al. 2015; Belli et al. 2015; Williams et al. 2017).

To identify PSBs at high redshift in greater numbers, two photometric methods have recently been developed. Whitaker et al. (2012) used medium-band near-infrared photometry to identify 'young red-sequence' galaxies from rest-frame *UVJ* colour–colour diagrams. Alternatively, Wild et al. (2014) established a classification scheme based on a Principal Component Analysis (PCA) of broad-band galaxy SEDs. Wild et al. (2014) apply their technique to the multiwavelength photometry of the Ultra Deep Survey (UDS; Almaini et al., in preparation), and find that just three shape parameters ('supercolours') provide a compact representation of a wide variety of SED shapes. This enables the separation of a tight red-sequence from star-forming galaxies, and also the identification of several unusual populations, e.g. PSBs, which are identified as galaxies that have formed a significant fraction of their mass in a recently-quenched starburst. This PCA technique has now led to the identification of > 900 PSBs in the UDS field at $0.5 < z < 2$ (see Wild et al. 2016). The validity of this method has also been confirmed using deep optical spectroscopy (Maltby et al. 2016). Of the photometrically-selected PSBs targeted for spectroscopic follow-up, ∼ 80 per cent show the expected strong Balmer absorption, (i.e. H$\,\delta$ equivalent width $W_{\mathrm{H}\,\delta} > 5$ Å, a general PSB diagnostic; see e.g. Goto 2007). Furthermore, the confirmation rate remains high (∼ 60 per cent), even when stricter criteria are used to exclude cases with significant [O II] emission. This is a more robust classification that ensures fewer star-forming contaminants, but excludes PSBs hosting AGN or with low levels of residual star formation.

For PSB galaxies, structural analyses can provide useful constraints on their evolutionary history and the likely mechanisms responsible for quenching their star formation. However, until recently, these analyses have largely been restricted to the Hubble-type morphologies of spectroscopic PSBs at $z < 1$ (e.g. Dressler et al. 1999; Caldwell et al. 1999; Tran et al. 2003; Poggianti et al. 2009; Vergani et al. 2010). In general, these studies find that, although PSBs are a morphologically heterogeneous population, they typically exhibit disc-like morphologies (e.g. S0/Sa). Fortunately, the recent development of photometric selection techniques has allowed the structure of these galaxies to be explored at $z > 1$, for the first time. For example, Almaini et al. (2017) examine the structure of massive ($M_* > 10^{10}\,M_\odot$) PSBs in the UDS at $z > 1$. They find that, in contrast to observations at lower redshift, these PSBs are spheroidally-dominated and exceptionally compact, with sizes typically smaller than older passive galaxies. They conclude that for massive PSBs at this epoch: i) morphological transformation has already taken place, occurring either before (or during) the quenching event; and ii) their results are consistent with the PSB phase being triggered by a gas-rich dissipative collapse, which quenched star formation and formed a compact remnant. Similar results have also been reported by Whitaker et al. (2012) and Yano et al. (2016), with young passive galaxies at $z > 1$ being more compact than their older counterparts. However, at intermediate redshifts ($z \sim 1$) there are currently conflicting results on the relationship between stellar age and the compactness of passive/recently-quenched galaxies (see e.g. Keating et al. 2015; Williams et al. 2017), and further study is required at this epoch.

In this paper, we build on previous results by using the PSB sample of Wild et al. (2016) to explore the structure of these galaxies, self-consistently, across a wide redshift range ($0.5 < z < 2$). For this we mainly use average (i.e. stacked) one-dimensional radial light $\mu(r)$ profiles obtained from the *Hubble Space Telescope* (*HST*) optical/near-infrared imaging available from the CANDELS survey (Grogin et al. 2011; Koekemoer et al. 2011). This work directly complements the study by Almaini et al. (2017), which uses the same parent PSB sample. We build on their recent results by extending the PSB structural analyses to: i) lower redshifts $z < 1$; ii) include *HST* optical imaging to probe younger stellar populations; and iii) consider galaxies with more complex structures (i.e. multiple components). Taken together, these structural analyses will aid in our understanding of the triggering mechanisms for the PSB phase, and of the mechanisms driving both the quenching and structural transformation of galaxies in the distant Universe.

The structure of this paper is as follows. In Section 2, we give a brief description of the data relevant to this work, and outline the PCA method used for identifying PSBs at high redshift. In Section 3, we describe the isophotal fitting technique used to obtain the one-dimensional radial light $\mu(r)$ profiles for our galaxies from the CANDELS optical/near-infrared imaging. Through Sections 4–6, we present various structural analyses using our $\mu(r)$ profiles for passive, star-forming and PSB galaxies at two different epochs ($0.5 < z < 1$ and $1 < z < 2$). We include a discussion of our results in Section 7, and draw our conclusions in Section 8. Throughout this paper, we use AB magnitudes and adopt a cosmology of $H_0 = 70\,\mathrm{km\,s^{-1}\,Mpc^{-1}}$, $\Omega_\Lambda = 0.7$ and $\Omega_\mathrm{m} = 0.3$.

2 DATA AND SAMPLE SELECTION

2.1 The Ultra Deep Survey (UDS)

This study is based on galaxy populations identified using the multiwavelength photometric data of the Ultra Deep Survey (UDS; Almaini et al., in preparation)[1]. This survey is the deepest component of the UKIRT (United Kingdom Infra-Red Telescope) Infrared

[1] http://www.nottingham.ac.uk/astronomy/UDS/

Deep Sky Survey (UKIDSS; Lawrence et al. 2007) and comprises extremely deep *JHK* photometry covering an area of 0.77 deg^2. In this work, we use the eighth UDS data release (DR8) where the limiting depths are $J = 24.9$, $H = 24.2$ and $K = 24.6$ (AB; 5σ in 2-arcsec apertures). The final UDS data release (DR11; June 2016), which achieved depths of $J = 25.4$, $H = 24.8$ and $K = 25.3$, will be used to extend our PSB studies in future work.

The UDS is complemented by extensive multiwavelength observations. These include, e.g. deep optical $BVRi'z'$ photometry from the Subaru–*XMM-Newton* Deep Survey (SXDS; Furusawa et al. 2008) and mid-infrared observations (3.6 and 4.5 μm) from the *Spitzer* UDS Legacy Program (SpUDS; PI: Dunlop). Deep optical u'-band photometry is also available from Megacam on the Canada-France-Hawaii Telescope (CFHT). The extent of the UDS field with full multiwavelength coverage (optical–mid-infrared) is ~ 0.62 deg^2. For a complete description of these data, including a description of the catalogue construction, see Hartley et al. (2013) and Simpson et al. (2012).

In this work, we use the photometric redshifts and stellar masses described in Simpson et al. (2013). These photometric redshifts ($z_{\rm phot}$) were determined by fitting the 11-band UDS photometry ($u'BVRi'z'JHK$, 3.6 μm and 4.6 μm) using a grid of galaxy templates built from Bruzual & Charlot (2003) stellar population models. The templates used had ages spaced logarithmically between 30 Myr and 10 Gyr, and included additional younger templates with dust-reddened SEDs. The quality of these $z_{\rm phot}$ measurements was confirmed by comparison to over 3000 secure spectroscopic redshifts $z_{\rm spec}$, with a normalized median absolute deviation $\sigma_{\rm NMAD} = 0.027$. Stellar masses were also determined by fitting the 11-band UDS photometry. This fitting used a large grid of synthetic SEDs from the stellar population models of Bruzual & Charlot (2003) and assumed a Chabrier (2003) initial mass function (IMF). Random errors in these stellar masses are typically ± 0.1 dex (see Simpson et al. 2013, for further details).

2.2 CANDELS–UDS

For our morphological analyses, we use the deep *HST* near-infrared/optical imaging from the CANDELS survey (Grogin et al. 2011; Koekemoer et al. 2011). This 902-orbit survey comprises Wide Field Camera 3 (WFC3) and parallel Advanced Camera for Surveys (ACS) imaging covering a total area of ~ 800 arcmin^2 spread across five survey fields. One of these fields was selected to target a sub-region of the UDS (CANDELS–UDS) and covers an area of ~ 210 arcmin^2 (~ 7 per cent of the UDS field). In this study, we focus mainly on the WFC3 near-infrared imaging ($J_{\rm F125W}$, $H_{\rm F160W}$) but also extend our analysis using the optical imaging from the ACS ($V_{\rm F606W}$, $I_{\rm F814W}$).

2.3 Sample selection

In this work, we use the large sample of UDS galaxies ($z > 0.5$) recently classified by Wild et al. (2016). These galaxies were classified using a photometric technique, developed by Wild et al. (2014), which is based on a Principal Component Analysis (PCA) of galaxy SEDs. We provide a brief overview of this method below.

The aim of the PCA technique is to describe a large variety of SED shapes through the linear combination of only a small set of principal components (i.e. shape parameters). In Wild et al. (2014, 2016), these components were derived from a large library of 'stochastic burst' model SEDs generated from Bruzual & Charlot (2003) stellar population synthesis models with stochastic star-formation histories. The result is a mean SED (m_λ) and a series of p eigenspectra $e_{i\lambda}$ (i.e. principal components) from which any normalised SED (f_λ/n) can be approximately reconstructed:

$$\frac{f_\lambda}{n} = m_\lambda + \sum_{i=1}^{p} a_i e_{i\lambda}. \quad (1)$$

The amplitudes of each component (a_i) indicate its contribution to the overall shape of the galaxy SED, and are referred to as '*supercolours*' (SCs). These SCs can be used to uniquely and succinctly define the shape of an SED, while retaining all the key information available from multiwavelength photometry. In fact, only the first three SCs are required to account for > 99.9 per cent of the variance in the models of Wild et al. (2014). Consequently, these three SCs alone can be used to provide a compact representation of a wide variety of SED shapes.

Various correlations exist between these SCs and the properties of the model SEDs, e.g. mean stellar age, dust content, metallicity and the fraction of mass formed in bursts in the last Gyr. These correlations enable the separation of a tight red-sequence from star-forming galaxies, as well as the identification of several unusual populations, e.g. i) very dusty star-forming galaxies; ii) metal poor quiescent dwarf galaxies, and iii) PSBs, which are selected as recently and rapidly quenched galaxies that have formed > 10 per cent of their mass within the last Gyr (see Maltby et al. 2016, for spectroscopic verification). We also separate the star-forming population into three sub-classes broadly reflecting an increase in luminosity-weighted mean stellar age, or decrease in specific star-formation rate (SF1 → SF2 → SF3). Although, note that these SF classes will suffer from the usual degeneracies between age and moderate amounts of dust and metallicity. With respect to the PSB selection, one important caveat is that not all those identified will necessarily have undergone the implied short-lived 'burst' of star formation prior to quenching, and that some may have experienced a more extended (≤ 3 Gyr) period of star formation that was rapidly quenched (see Wild et al. 2016, for further details). Nonetheless, this population as a whole does represent transient galaxies that have been recently and rapidly quenched (which is what we are primarily interested in), and we simply retain the PSB nomenclature here for consistency with previous works in the series (Wild et al. 2014, 2016; Maltby et al. 2016; Almaini et al. 2017; Socolovsky et al. 2018).

To classify real galaxies, SCs are calculated by projecting their SEDs onto the PCA eigenspectra. These SCs are then compared with those of the model SEDs in order to determine the galaxy's most probable nature (e.g. red-sequence, star-forming, PSB). The benefit of this approach is that the SCs of real galaxies are independent of model-fitting and free to have values that differ substantially from those of the input model library. In the UDS field, this PCA analysis utilises 8 UDS filters ($VRi'z'JHK$, 3.6 μm; a filter set which optimises the principal components for PSB identification), and is performed on all galaxies with $K_{\rm AB} < 24$ and $0.5 < z < 2.0$ (48 713 galaxies; Wild et al. 2016). This resulted in a large parent sample of 4249 red-sequence (or 'passive') galaxies, 39 970 star-forming galaxies and 921 PSBs.

In this work, we use CANDELS *HST* imaging for our morphological analyses. Approximately 10 per cent of our parent galaxy sample lies within the CANDELS–UDS field and has available *HST* imaging. This provides a final sample of 429 passive galaxies, 3579 star-forming galaxies (2278 SF1, 761 SF2, 540 SF3) and 98 PSB galaxies. We use this sample of CANDELS galaxies throughout this study.

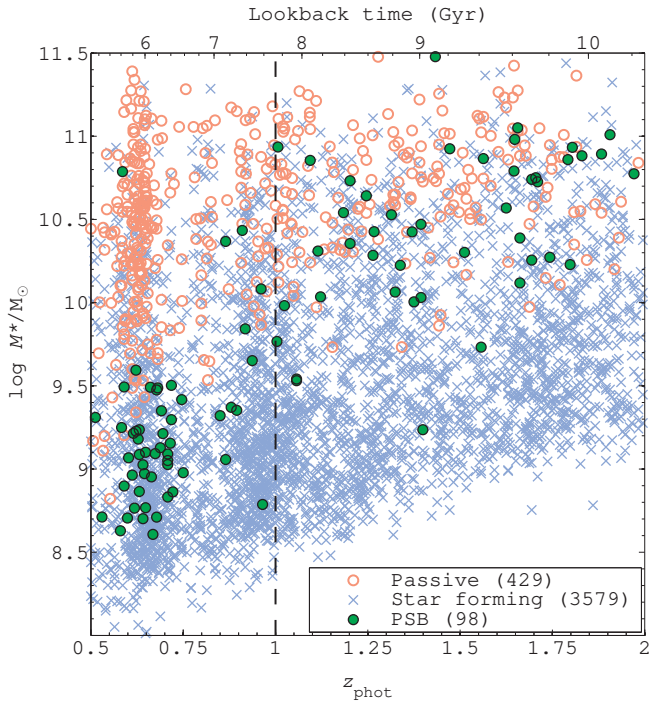

Figure 1. The stellar mass M_* distribution as a function of photometric redshift for passive (red circles), star-forming (blue crosses) and PSB galaxies (green points), within the CANDELS–UDS field. Respective sample sizes are shown in the legend. For PSB galaxies, there is significant evolution in the stellar mass distribution over $0.5 < z < 2$ (see Wild et al. 2016, for further details). In this paper, we take this evolution into account by considering the structural properties of these galaxies at two different epochs: $0.5 < z < 1$ and $1 < z < 2$ (separated by the black dashed line).

2.4 Stellar mass distributions

In Fig. 1, we present the stellar mass M_* distribution as a function of redshift for passive, star-forming and PSB galaxies, within the CANDELS–UDS field. This clearly indicates that for PSBs, there is a strong evolution in the M_* distribution across $0.5 < z < 2$. PSBs at $z < 1$ are generally of low stellar mass ($M_* < 10^{10}\,\mathrm{M}_\odot$), while at higher redshift ($z > 1$) they are typically of high stellar mass ($M_* > 10^{10}\,\mathrm{M}_\odot$). Wild et al. (2016) recently reported this evolution in the PSB mass function using the SC-classified galaxies from the entire UDS field (i.e. our parent galaxy sample; see Section 2.3). Their results indicate that the comoving space density of massive PSBs ($M_* > 10^{10}\,\mathrm{M}_\odot$) is $\sim 10\times$ higher at $z \sim 2$ than at $z \sim 0.5$ (see Whitaker et al. 2012, for a similar result). Furthermore, at $z > 1$ the clear turnover in the PSB mass function towards low M_* (see Wild et al. 2016, figure 4), suggests that the absence of low-mass PSBs at $z > 1$ is likely to be genuine, and not just an effect of mass-incompleteness. However, this issue will be explored in more depth in a future study, using the deeper UDS DR11 data (Wilkinson et al., in preparation). Taken together, these results suggest that PSBs at $z > 1$ are likely to be a different population to those observed at lower redshifts, potentially with different evolutionary histories, and with the PSB phase being triggered by different mechanisms. Consequently, in this study, we account for this evolution in the M_* distribution by examining PSB structure in two separate epochs: intermediate-z ($0.5 < z < 1$) and high-z ($1 < z < 2$).

For both epochs, we also assess whether our sample of CANDELS galaxies is representative of those from the wider UDS field (see Section 2.3). For each galaxy population, we compare the M_* and redshift distributions between these two fields, and find no significant differences in most cases (based on Kolmogorov-Smirnov tests; $p > 0.01$). The only exceptions are for the redshift distributions of passive and PSB galaxies at $0.5 < z < 1$, where we find an excess in the CANDELS samples at $z \sim 0.65$. This is due to a known supercluster in this field (see e.g. van Breukelen et al. 2006; Galametz et al. 2018), and therefore environmental effects may be particularly relevant for our galaxy samples at this epoch. We return to this point in Section 7.2.

Table 1. The mass-limited galaxy samples used throughout this work, including the sub-samples for the star-forming population (SF1, SF2, SF3).

Sample	N(intermediate-z) $0.5 < z < 1.0$ $M_* > 10^9\,\mathrm{M}_\odot$	N(high-z) $1.0 < z < 2.0$ $M_* > 10^{10}\,\mathrm{M}_\odot$
Passive	256	165
Star forming	883	536
SF1	404	54
SF2	265	192
SF3	214	290
PSB	36	39

In this work, our galaxy samples are derived from the SC analysis of Wild et al. (2016), which was performed on UDS galaxies with $K < 24$ (see Section 2.3). Using this K limit, the equivalent mass-completeness limits were determined as a function of redshift using the method of Pozzetti et al. (2010). For galaxies in the CANDELS–UDS field, we find that completeness is $\gtrsim 95$ per cent for the following mass ranges: $M_* > 10^9\,\mathrm{M}_\odot$ ($0.5 < z < 1$) and $M_* > 10^{10}\,\mathrm{M}_\odot$ ($1 < z < 2$). These mass limits are used throughout this work. Note, that since mass–completeness varies smoothly across redshift, these limits are conservative and strictly only applicable at the upper-z limit of each epoch. This is particularly important when considering the high-z epoch, where a lower mass limit of $M_* > 10^{9.5}\,\mathrm{M}_\odot$ would actually yield equivalent completeness over $1 < z < 1.5$. The sizes of the final mass-limited galaxy samples used throughout this work, are presented in Table 1.

3 RADIAL LIGHT PROFILES

In this section, we describe the measurement of galaxy radial light $\mu(r)$ profiles from the CANDELS *HST* imaging and the production of stacked $\widetilde{\mu}(r)$ profiles. The relevant profile fitting and structural analyses are presented in Sections 4–6.

In this work, we stack one-dimensional radial $\mu(r)$ profiles, which enables us to maximise signal-to-noise, particularly for the outer galactic regions. This is desirable for the reliable multi-component decomposition of our faint galaxies, and necessary for the identification of faint components (e.g. outer discs) that may not be detected in individual profiles. This one-dimensional approach has the advantage of providing a simple visualisation of the true galactic structure (i.e. non-parametrised) for comparison to fitted $\mu(r)$ profiles. This can be useful for determining whether an extra component (e.g. outer disc) is really present. We are aware that the inherent loss of azimuthal information could introduce some uncertainty to the fitted structural parameters, and an alternative approach would be to use two-dimensional analyses (i.e. stack galaxy images). However, the differences in results between a one- and two-dimensional analysis are minimal. For face-on galaxies the two

methods will yield the same results, and for inclined galaxies, single Sérsic and disc parameters (and most bulge parameters) will be consistent within fitting errors in most cases, with a characteristic scatter at the 10–20 per cent level (see e.g. de Jong 1996; MacArthur et al. 2003; McDonald et al. 2011). In this work, we choose to adopt the one-dimensional approach, but we also independently confirm that these two methods would lead to consistent results for our samples (see Section 4.2).

3.1 Isophotal fitting

For each galaxy, we use the IRAF task ellipse[2] in order to obtain their azimuthally-averaged radial light $\mu(r)$ profiles from the CANDELS ACS/WFC3 imaging (see Jedrzejewski 1987). This isophotal fitting was performed independently in each of the four CANDELS wavebands ($V_{\rm F606W}$, $I_{\rm F814W}$, $J_{\rm F125W}$ and $H_{\rm F160W}$).

In our isophotal fitting, bad pixel masks were used to remove all potential sources of contamination, e.g. background/companion galaxies and foreground stars (anything not associated with the subject galaxy itself). These masks were created from SExtractor segmentation maps, and a separate mask was generated for each CANDELS waveband. A validation of these masks was also performed by visual inspection to ensure that all potential sources of contamination were adequately masked; see Fig. 2 for a typical example.

To determine the radial $\mu(r)$ profiles, free-parameter isophotal fits were performed for each galaxy (fixed centre, free ellipticity e and position angle PA). These fits tend to follow significant morphological features (e.g. bulges, bars, spiral arms) and are consequently suitable for tracing a galaxy's principal structural component (i.e. bulge and/or disc). In these isophotal fits, we use linear radial sampling ($\Delta r = 0.1$ pixel, where r is the radius along the semi-major axis) and a fixed isophotal centre determined for each galaxy by SExtractor. In isophotal fitting, it is often advisable to begin the fitting procedure from a good initial estimate for an inner isophote. To provide this initial isophote, we use the shape parameters (e, PA) obtained for our galaxies from SExtractor. In our isophotal fits, four iterations of a 3σ rejection are also applied to deviant points along each isophote to remove the influence of non-axisymmetric features on the resultant $\mu(r)$ profile (i.e. star-forming regions and supernovae). A typical example of an isophotal fit for one of the PSB galaxies is presented in Fig. 2.

3.2 Sky subtraction

With isophotal analyses, it is very important to perform a careful sky subtraction to remove the effect of the sky/background on the resultant $\mu(r)$ profile. The slight under-/over-subtraction of the sky can easily lead to an incorrect profile shape, particularly in the outer regions of the profile (see Maltby et al. 2012a,b, 2015, for some recent studies). The publicly available CANDELS *HST* WFC3/ACS imaging have already undergone a careful sky subtraction (Koekemoer et al. 2011) and residual sky in these images is not expected to be significant. Nonetheless, we measure the residual sky level in the WFC3/ACS images in order to assess the potential influence on the shape of our $\mu(r)$ profiles.

For each galaxy in our sample, we obtain an estimate of the local sky background ($n_{\rm sky}$) by using pixels obtained from the four corners of the galaxy WFC3/ACS image (i.e. postage stamp). The sizes of these postage stamps are variable and designed to optimally contain the subject galaxy. The size is based on a multiple of the Kron (1980) radius ($\sim 4\times$), and therefore from theoretical light profiles these postage stamps should contain > 98 per cent of the subject galaxy's light (see e.g. Bertin & Arnouts 1996). As a consequence, in sampling the corners of these postage stamps we have a reasonable expectation of probing the actual sky background. The corner image pixels were selected using quarter-circle wedges of side equal to 10 per cent of the smallest image dimension (corresponding to a region > 3.6 Kron radii from the galaxy's centre). We then apply our bad pixel masks to ensure only 'dark' pixels are used and obtain the median pixel value $\widetilde{n_{\rm e}}$ (or 'sky level') in each wedge. The mean of these sky levels from the four corners of the galaxy postage stamp is then used as a local estimate of the residual sky background ($n_{\rm sky}$). For each galaxy postage stamp, the corner-to-corner rms in their four $\widetilde{n_{\rm e}}$ measurements is also determined and taken as an estimate for the 1σ error in the local sky background $\sigma_{\rm sky}$ (i.e. the local error in the sky subtraction).

For the near-infrared imaging ($J_{\rm F125W}$, $H_{\rm F160W}$), the residual sky level was determined to be well below tolerance levels, with the average sky level at least two orders of magnitude below a typical $\mu(r)$ profile at the limiting galactocentric radius used in this study ($r_{\rm lim} = 1.6$ arcsec). This limiting radius is defined as the threshold at which a typical $\mu(r)$ profile enters the region dominated by uncertainly in the sky background (i.e. the flux limit corresponding to the average sky subtraction error $\widetilde{\sigma}_{\rm sky}$). However, for the optical imaging ($V_{\rm F606W}$, $I_{\rm F814W}$), the residual sky level is much higher than in the near-infrared, and potentially a significant component of the $\mu(r)$ profile at $r_{\rm lim}$ (possibly accounting for up to ~ 20 per cent of the flux). To address this issue, we correct all our optical/near-infrared $\mu(r)$ profiles by subtracting the corresponding local residual sky background $n_{\rm sky}$ on a galaxy-galaxy basis.

3.3 PSF determination

Point spread functions (PSFs) for the CANDELS *HST* imaging are well determined and have FWHM varying between 0.08–0.18 arcsec (Koekemoer et al. 2011). However, at the redshifts studied in this work ($z > 0.5$), the half-light radii of galaxies are typically < 1 arcsec (see e.g. Almaini et al. 2017). Consequently, the *HST* PSF can be a considerable factor in the $\mu(r)$ profiles of our galaxies (see Fig. 2, for an example). The determination of an accurate PSF and its influence on our $\mu(r)$ profiles is therefore critical to the measurement of reliable structural properties ($r_{\rm e}$, n) in this work.

To construct our PSFs, we use isolated stars identified in the UDS field (see Lani et al. 2013; Almaini et al. 2017) that reside within the CANDELS–UDS region (~ 150 stars). For each CANDELS waveband, we create postage stamps for these stars (stamp size: 4×4 arcsec^2), which are then normalised in total flux (aperture diameter = 2.828 arcsec) and combined in a median stack. The resultant PSF images reveal significant structural features that could easily affect our galaxy $\mu(r)$ profiles (e.g. diffraction spikes and Airy rings). To illustrate this, we use isophotal fitting to generate radial $\mu(r)$ profiles from our PSF images (see Fig. 3). These profiles also show that the PSF structure changes considerably between the different CANDELS wavebands. As expected, the WFC3 PSFs ($J_{\rm F125W}$, $H_{\rm F160W}$) are broader than the ACS PSFs ($V_{\rm F606W}$, $I_{\rm F814W}$), but they also exhibit more prominent Airy rings that manifest as significant bumps in their radial $\mu(r)$ profiles. In this work, we use the PSF images determined here to account for the nature of the CANDELS PSFs in our structural analyses (see Section 4).

[2] STSDAS package – version 3.14

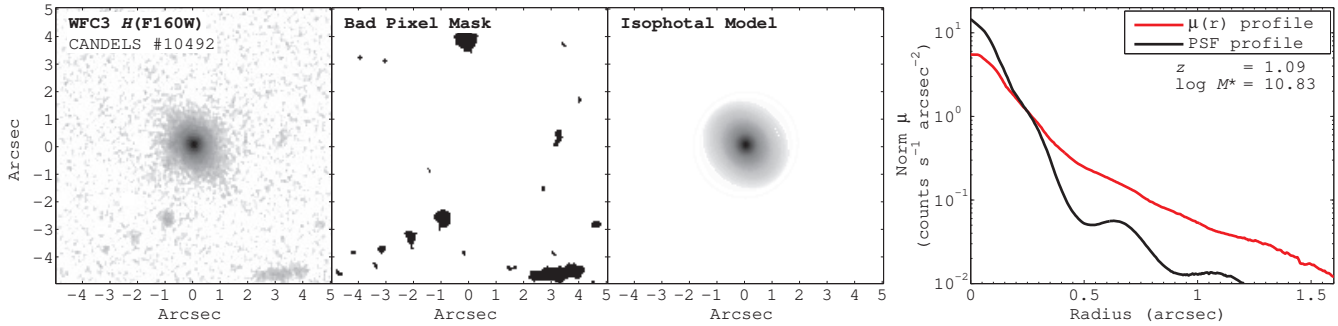

Figure 2. An example isophotal fit for a typical post-starburst galaxy. Left-hand panel: *HST*/WFC3 $H_{\rm F160W}$ image. Centre-left panel: the bad pixel mask used for the isophotal fit. Centre-right panel: the isophotal model generated by ellipse. Right-hand panel: the resultant azimuthally-averaged radial light $\mu(r)$ profile (red line), with the *HST*/WFC3 $H_{\rm F160W}$ PSF profile (black line) also shown for reference. Both profiles have been normalised using the flux contained within a 2.828 arcsec aperture.

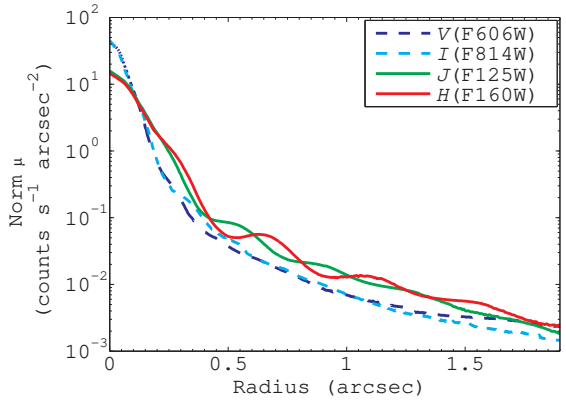

Figure 3. The CANDELS *HST* PSFs. Radial light $\mu(r)$ profiles for the CANDELS PSFs, showing the differences in structure between the four wavebands. These PSFs have been empirically determined from isolated stars in the CANDELS *HST* images. All profiles have been normalised using the flux contained within a 2.828 arcsec aperture.

3.4 Stacked light profiles $\widetilde{\mu}(r)$

To assess the general structure of PSB galaxies, we combine their individual $\mu(r)$ profiles in median stacks. This is performed separately in each CANDELS waveband and for our samples at the two different epochs, $0.5 < z < 1$ and $1 < z < 2$. Analogous median stacks are also generated for the passive and star-forming galaxies. We give a brief description of the stacking procedure below.

To generate our median stacked profiles $\widetilde{\mu}(r)$, we take the median flux of the respective sample of individual $\mu(r)$ profiles as a function of radius. The individual $\mu(r)$ profiles were normalised in flux prior to stacking (using the flux within a 2.828 arcsec aperture). During the stacking process, we also perform one iteration of a 3σ clip to individual $\mu(r)$ profiles that deviate from the median flux within the limiting galactocentric radius ($r_{\rm lim}$ = 1.6 arcsec; see Section 3.2). Clipping is not performed beyond $r_{\rm lim}$ due to the increased level of uncertainty in the individual $\mu(r)$ profiles as they approach the limit of the background noise. This clipping improves the 1σ error boundaries on our $\widetilde{\mu}(r)$ profiles, but has no significant effect on their overall shape (i.e. structural parameters). Note that we do not normalise for apparent size (i.e. angular extent) in our stacking analysis, since this would also destandardize the significant effect of the PSF (see Section 3.3). However, from an assessment of simulated $\widetilde{\mu}(r)$ stacks, we find this normalisation to be unnecessary.

We also note that for the two epochs studied, the change in angular scale (kpc arcsec^{-1}) with redshift has no significant influence on the shape of the resultant $\widetilde{\mu}(r)$ profiles (see Section 4.1).

For each galaxy population, the $\widetilde{\mu}(r)$ profiles from the CANDELS $H_{\rm F160W}$ imaging are presented in Fig. 4. Random errors in these $\widetilde{\mu}(r)$ profiles (1σ) are the error in the median flux as a function of radius, which is determined from the mean of the standard errors from 100 simulated stacks generated via a bootstrap method. Virtually identical $\widetilde{\mu}(r)$ profiles were also obtained from the $J_{\rm F125W}$ imaging. For the optical imaging ($V_{\rm F606W}$, $I_{\rm F814W}$), the $\widetilde{\mu}(r)$ profiles are presented in Section 6.

An inspection of our $H_{\rm F160W}$ $\widetilde{\mu}(r)$ profiles reveals some significant differences in structure between the different populations (see Fig. 4). For both epochs, the passive and PSB populations have stellar distributions that appear more compact and centrally concentrated than the star-forming population (see Williams et al. 2010 and van der Wel et al. 2014, for similar results). The PSB population also appears to have stellar distributions that are marginally more compact than the passive population, particularly at high redshift ($1 < z < 2$). In the following sections, we perform profile fitting on these profiles to analyse their structure in more detail.

4 PROFILE FITTING

To determine structural properties from the average $\widetilde{\mu}(r)$ profiles (e.g. effective radius $r_{\rm e}$; Sérsic index n), we perform one-dimensional profile fitting via the comparison of these measured profiles to a large library of $\sim$ 22 000 model galaxy profiles.

To build the model library, we begin by generating mock galaxy images using two-dimensional Sérsic models that cover a wide range of profile shapes ($0.7 < n < 8$; $0.01 < r_{\rm e} < 1.5$ arcsec). Each image was then convolved with the relevant *HST* PSF (see Section 3.3) and normalised in total flux. Free-parameter isophotal fits (fixed centre, free ellipticity e and position angle PA) were then performed to generate the azimuthally-averaged radial light profiles which comprise the model library $\{\mu_{\rm mock}(r)\}$. These isophotal fits are analogous to those described for our measured light $\mu(r)$ profiles in Section 3.1. A separate model library is generated for each CANDELS waveband ($V_{\rm F606W}$, $I_{\rm F814W}$, $J_{\rm F125W}$, $H_{\rm F160W}$), in order to take account of the significant differences observed in the structure of their PSFs (see Section 3.3; Fig. 3).

For profile fitting (single Sérsic), a measured light profile is compared to every profile in the relevant model library and the best-fit is obtained by χ^2 minimisation. The measured/model profiles are

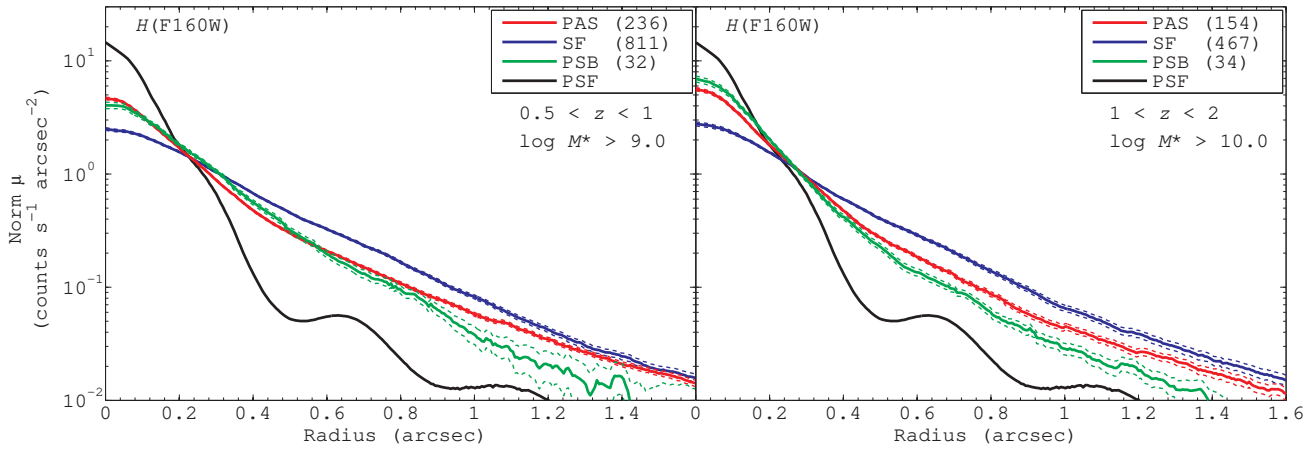

Figure 4. Median-stacked $H_{\rm F160W}$ light profiles $\widetilde{\mu}(r)$ for different galaxy populations and at different epochs. Left-hand panel: $\widetilde{\mu}(r)$ profiles for passive (PAS; red line), star-forming (SF; blue line) and PSB galaxies (green line) at $0.5 < z < 1$. Right-hand panel: analogous $\widetilde{\mu}(r)$ profiles at $1 < z < 2$. The errors in the $\widetilde{\mu}(r)$ profiles (dashed lines) are 1σ confidence limits, which are determined from the mean of the standard errors from 100 simulated stacks generated via a bootstrap method. The respective sample sizes used to generate the $\widetilde{\mu}(r)$ profiles are shown in the legend. The *HST* $H_{\rm F160W}$ PSF profile (black line) is also shown for reference. Virtually identical $\widetilde{\mu}(r)$ profiles are also obtained from the $J_{\rm F125W}$ imaging.

resampled ($0.1\times$ sample rate) to ensure the data points used in the χ^2 minimisation are radially independent. The full library for the relevant waveband is also used in each fit, to ensure a global minimum solution is obtained. During this process the normalisation of the model profiles are allowed to vary. This is necessary to ensure the best-fit is only defined by the 'shape' of the profile, and not by slight differences in the normalisation between the measured and model profiles. For fitting purposes, we only use data from $r < r_{\rm lim}$ ($r_{\rm lim} = 1.6$ arcsec; see Section 3.2) to ensure the fit is driven by the main structural components (bulge/disc) and not affected by any uncertainty in the sky subtraction.

In the following Sections (4.1–5), we focus in detail on the profile fitting results for the near-infrared $\mu(r)$ profiles (WFC3 – $J_{\rm F125W}$, $H_{\rm F160W}$). The profile fitting results for the optical $\mu(r)$ profiles (ACS – $V_{\rm F606W}$, $I_{\rm F814W}$) will be discussed in Section 6. In this work, we are mainly interested in the general structure of our galaxies stellar distributions. For our galaxies ($z > 0.5$), the near-infrared directly probes the old stellar component ($\lambda_{\rm rest} > 4000$ Å), which comprises the bulk of the stellar mass. Therefore, the near-infrared $\mu(r)$ profiles are the principal focus of this study.

4.1 Stacked light profiles $\widetilde{\mu}(r)$

For each galaxy population, we perform single Sérsic fits on the median-stacked light profiles $\widetilde{\mu}(r)$ and obtain their typical structural properties (i.e. $r_{\rm e}$, n). The resultant fits for the $H_{\rm F160W}$ $\widetilde{\mu}(r)$ profiles are shown in Fig. 5. In all cases, the $\widetilde{\mu}(r)$ profiles are well described by a single Sérsic profile, with the best fit having a reduced chi-squared $\chi^2_{\rm red} \sim 1$. Furthermore, the χ^2 distribution for fits across the full $r_{\rm e}$–n parameter space shows that these best-fits are stable, well defined and that no degeneracies are present. Very similar results are also obtained for the $J_{\rm F125W}$ $\widetilde{\mu}(r)$ profiles. The resultant structural parameters ($r_{\rm e}$, n) for each galaxy population in both $J_{\rm F125W}$ and $H_{\rm F160W}$, are shown in Table 2. The uncertainty in these structural parameters (1σ) is estimated, independently for each galaxy population, using the variance between analogous fits performed on 100 simulated $\widetilde{\mu}(r)$ profile stacks generated via a bootstrap analysis. For estimates of the effect of the PSF and sky subtraction error $\widetilde{\sigma}_{\rm sky}$ on these measurements, see Section 4.2.

Fig. 6 (a/b) shows a comparison of the $H_{\rm F160W}$ $\widetilde{\mu}(r)$ structural properties ($r_{\rm e}$, n) for each galaxy population and for the two epochs ($0.5 < z < 1$ and $1 < z < 2$). A similar comparison of the $J_{\rm F125W}$ $\widetilde{\mu}(r)$ profiles yields entirely consistent results, with respect to the errors (see Table 2). For both epochs, the general structure of the passive and star-forming populations are as expected. Passive galaxies are compact [$0.2 < r_{\rm e} < 0.3$ arcsec (1.7–2 kpc)] and have high Sérsic indices ($n \sim 3.3$), indicating their spheroidal nature. In contrast, star-forming galaxies have significantly more extended stellar distributions [$r_{\rm e} > 0.3$ arcsec (> 2.7 kpc)] with the lower Sérsic indices ($1 < n < 2$) typical of their disc-dominated structures. For the star-forming sub-populations (SF1, SF2, SF3) at both epochs, we observe a slight increase in Sérsic index from SF1 $\rightarrow$ SF3 (i.e. with increasing mean stellar age), while at $z > 1$ we also observe a significant decrease in size [$r_{\rm e} \sim 0.5 \rightarrow 0.3$ arcsec ($4.2 \rightarrow 2.6$ kpc)]. This trend suggests an increase in the dominance of the bulge component towards older star-forming galaxies. Interestingly, for PSB galaxies we observe significant differences in their structure at different epochs. At $z > 1$, the PSBs are extremely compact [$r_{\rm e} \sim 0.13$ arcsec (~ 1.1 kpc)] and of high Sérsic index ($n \sim 3.2$), with structures similar to the passive population but considerably more compact (by ~ 40 per cent). In contrast, at $z < 1$ the PSBs have significantly different structures. At this epoch, PSBs are still relatively compact [$r_{\rm e} \sim 0.22$ arcsec (~ 1.6 kpc)], but exhibit much lower Sérsic indices ($n \sim 1.7$) than the PSBs at $z > 1$.

With respect to these results, it is important to take into consideration the mass distributions of the respective galaxy populations (see Fig. 1), due to the well-established correlations between mass and galaxy structure (e.g. the mass–size relation; Shen et al. 2003). At high redshift ($z > 1$), our galaxies are all of high mass ($M_* > 10^{10}\,{\rm M}_\odot$) and have relatively similar mass distributions. Nonetheless, in our high-z $\widetilde{\mu}(r)$ profiles it is possible that PSBs appear more compact than the passive population due to slight differences in their respective mass distributions. To address this issue, we repeat our high-z analysis using two narrower mass bins ($10^{10} < M_* < 10^{10.5}\,{\rm M}_\odot$ and $10^{10.5} < M_* < 10^{11}\,{\rm M}_\odot$). In both cases, PSBs remain significantly more compact than the passive population, and we observe the same trends in our $\widetilde{\mu}(r)$ structural parameters (with respect to the errors). Consequently, we conclude

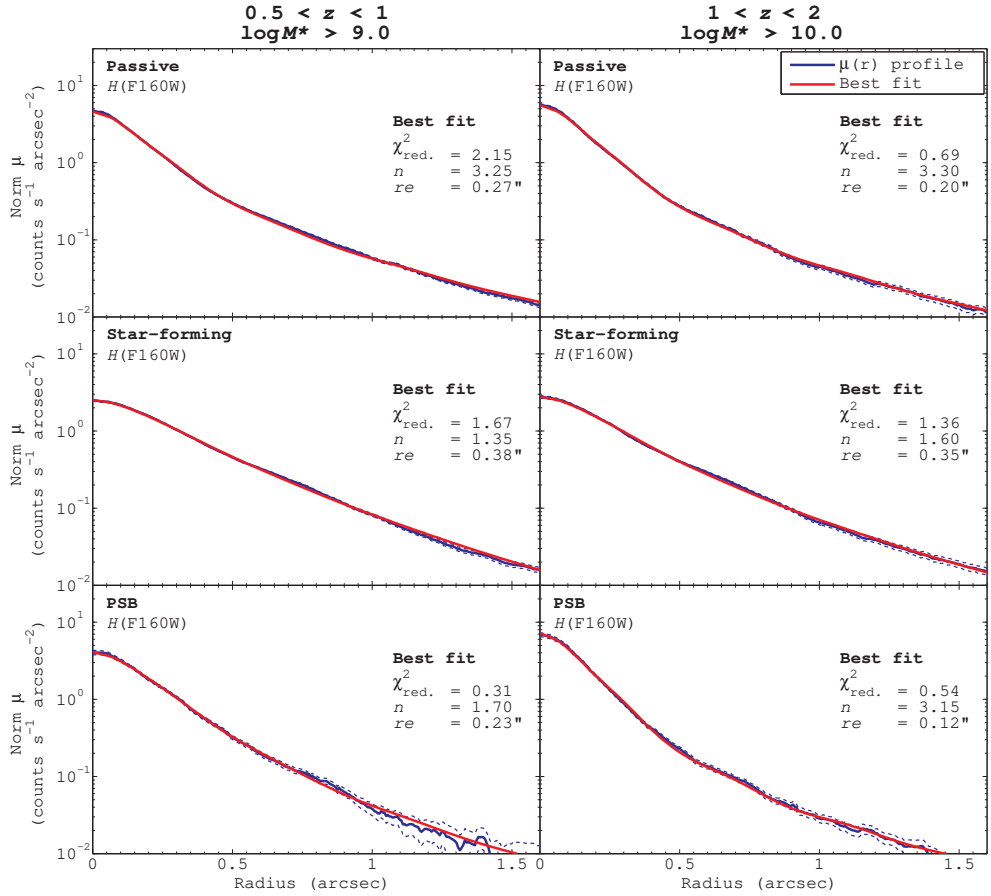

Figure 5. Single Sérsic fits to our median-stacked $H_{\rm F160W}$ light profiles $\widetilde{\mu}(r)$ from two separate epochs: $0.5 < z < 1$ (left-hand column) and $1 < z < 2$ (right-hand column). In all cases (passive, star-forming, PSB), our $\widetilde{\mu}(r)$ profiles are well described by a single Sérsic profile. Virtually identical fits are also obtained from our $J_{\rm F125W}$ $\widetilde{\mu}(r)$ profiles (see Table 2).

Table 2. Near-infrared single Sérsic fits: the structural properties for our median-stacked $J_{\rm F125W}$ and $H_{\rm F160W}$ light profiles $\widetilde{\mu}(r)$. Structural properties ($r_{\rm e}$, n) are shown for different galaxy populations (passive, star-forming, PSB) at two different epochs, $0.5 < z < 1$ and $1 < z < 2$. Errors in the structural parameters (1σ) are determined from the variance between fits performed on 100 simulated $\widetilde{\mu}(r)$ profile stacks generated via a bootstrap method.

Galaxy Population	$0.5 < z < 1$				$1 < z < 2$			
	$J_{\rm F125W}$		$H_{\rm F160W}$		$J_{\rm F125W}$		$H_{\rm F160W}$	
	n	$r_{\rm e}$ (arcsec)	n	$r_{\rm e}$ (arcsec)	n	$r_{\rm e}$ (arcsec)	n	$r_{\rm e}$ (arcsec)
Passive	3.25 ± 0.15	0.28 ± 0.01	3.25 ± 0.15	0.27 ± 0.01	3.20 ± 0.18	0.21 ± 0.01	3.30 ± 0.19	0.20 ± 0.01
Star-forming	1.30 ± 0.05	0.39 ± 0.01	1.35 ± 0.04	0.38 ± 0.01	1.65 ± 0.10	0.37 ± 0.01	1.60 ± 0.06	0.35 ± 0.01
SF1	1.10 ± 0.04	0.40 ± 0.01	1.15 ± 0.05	0.38 ± 0.01	1.20 ± 0.16	0.52 ± 0.06	1.20 ± 0.14	0.47 ± 0.06
SF2	1.35 ± 0.08	0.39 ± 0.02	1.35 ± 0.07	0.38 ± 0.02	1.45 ± 0.12	0.43 ± 0.02	1.40 ± 0.10	0.41 ± 0.02
SF3	1.70 ± 0.12	0.38 ± 0.02	1.70 ± 0.11	0.36 ± 0.02	1.95 ± 0.13	0.32 ± 0.01	1.85 ± 0.13	0.30 ± 0.01
Post-starburst	1.70 ± 0.20	0.22 ± 0.01	1.70 ± 0.24	0.23 ± 0.01	3.65 ± 0.32	0.13 ± 0.01	3.15 ± 0.34	0.12 ± 0.01

that any slight differences in the mass distributions of our samples have no significant effect on our results for $z > 1$.

In contrast, at lower redshift ($0.5 < z < 1$), there are more significant differences between the mass distributions of our galaxy samples. At this epoch, PSBs are generally of low stellar mass ($10^9 < M_* < 10^{10}\,{\rm M}_\odot$), while the passive and star-forming populations have a wide range of masses ($10^9 < M_* < 10^{11.5}\,{\rm M}_\odot$). Therefore, to perform a fair comparison at this epoch, we need to match the passive and star-forming galaxies to a mass range comparable to the PSB population (i.e. $10^9 < M_* < 10^{10}\,{\rm M}_\odot$). Fig. 6 (c) shows the structural parameters for the resultant mass-matched $\widetilde{\mu}(r)$ profiles. For the general star-forming population, restricting the mass range has little effect on their typical structural properties. However, there is a significant change in the general structure of the passive population, which now resembles that of PSBs [$r_{\rm e} \sim 0.2$ arcsec (~ 1.5 kpc), $n \sim 2$]. Therefore, we conclude that at this epoch, PSBs have similar structures to those of the low-mass passive population (i.e. passive discs), the population into which they will most likely evolve. We explore this result in more detail in the following sections. We note that the low-mass SF3 population also resembles

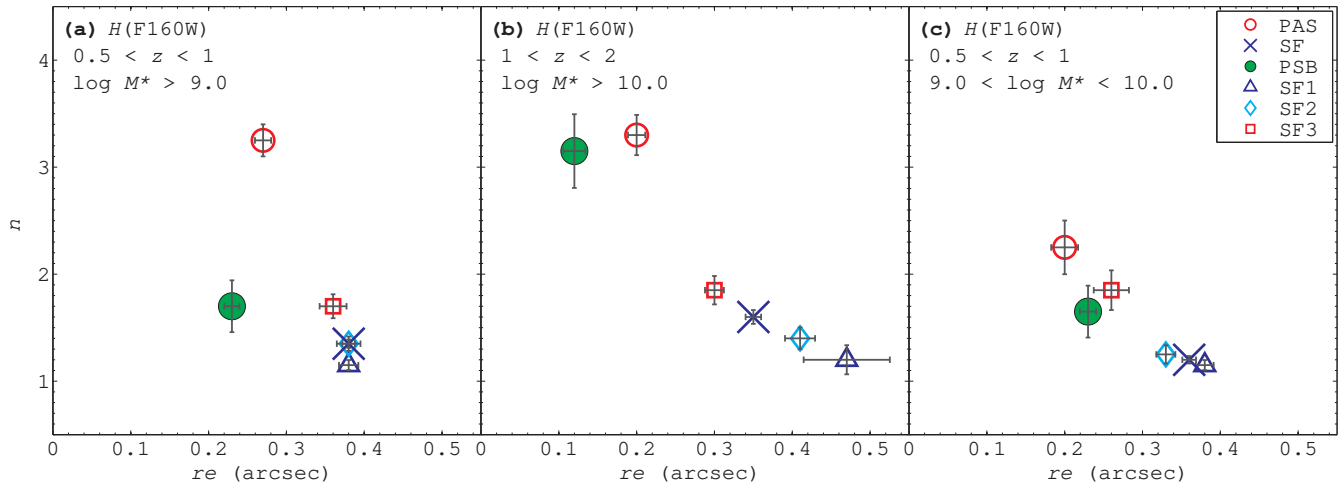

Figure 6. Structural properties (effective radius r_e, Sérsic index n) from the single Sérsic fits to our median-stacked H_{F160W} light profiles $\widetilde{\mu}(r)$ – see Table 2. Left-hand panel (a): the typical structural properties for passive (PAS), star-forming (SF) and PSB galaxies at $0.5 < z < 1$. The structural properties for the star-forming sub-populations (SF1 → SF3; based on decreasing sSFR), are also shown. Centre panel (b): analogous results for $1 < z < 2$. These results reveal significant differences in the structure of PSBs at different epochs. At $z > 1$, PSBs are extremely compact and of high n, with structures similar to the passive population but more compact. However, at $z < 1$, PSBs are relatively compact but exhibit much lower n than the PSBs at $z > 1$. Right-hand panel (c): the results for low-z ($0.5 < z < 1$) when the galaxy samples have been limited to a mass range comparable to the PSB population (i.e. low-mass; $10^9 < M_* < 10^{10}\,M_\odot$). This shows that PSBs at this epoch have structures that are very similar to both the low-mass passive and SF3 populations. Errors in the structural parameters (1σ) are determined from the variance between fits performed on 100 simulated $\widetilde{\mu}(r)$ profile stacks generated via a bootstrap method. For all populations studied, the H_{F160W} structural parameters are entirely consistent with those obtained from the J_{F125W} $\widetilde{\mu}(r)$ profiles (see Table 2).

PSBs in structure, but since these galaxies are unlikely to be PSB progenitors (due to their low sSFR; see Section 2.3), we do not consider this result any further.

For each epoch studied ($0.5 < z < 1$ and $1 < z < 2$), it is also important to consider any differences in the redshift distributions between the galaxy populations (see Fig. 1), due to the potential for structural evolution across the epoch. A further consideration is the angular scale, which over $1 < z < 2$ is relatively constant (~ 8.5 kpc arcsec^{-1}), but for $0.5 < z < 1$ varies more significantly (6–8 kpc arcsec^{-1}). To address these issues, we split both the intermediate- and high-z epochs into two narrower sub-epochs and assess the effect on our $\widetilde{\mu}(r)$ profiles. These sub-epochs are redshifts 0.5–0.75 and 0.75–1.0 for the intermediate-z epoch, and 1.0–1.5 and 1.5–2.0 for the high-z epoch. For both the intermediate- and high-z epochs, we find no significant differences in the structural parameters between the respective sub-epochs for each galaxy population (with respect to the errors; see Table 2). The only exceptions are: i) high-z passive and PSB galaxies, where there is a slight indication of a higher Sérsic index n at $1 < z < 1.5$ than at $1.5 < z < 2$, but this has no significant effect on the overall trends observed; and ii) intermediate-z galaxies, where we find some minor differences in effective radius (in arcsec) between the two sub-epochs ($\delta r_e < 0.05$ arcsec), as might be expected. However, these differences equate to a change in the physical effective radius of < 0.15 kpc, and consequently have no significant effect on the overall trends for the $0.5 < z < 1$ epoch presented here.

4.2 Further robustness tests

In this study, a careful treatment of the PSF is critical for determining structural properties (r_e, n), particularly for compact galaxy populations (e.g. PSBs). In our profile fitting, we take account of the PSF by using a library of PSF-convolved models (see Section 4). Nonetheless, we assess whether PSF effects could cause a bias in our fitted structural parameters by adopting a similar method to that developed by Szomoru et al. (2010, 2012), and deconvolve our $\widetilde{\mu}(r)$ profiles for the PSF. To achieve this, we first calculate a residual profile $\widetilde{\mu}_{res}(r)$ by subtracting our best fit profile (which is PSF-convolved) from the median-stacked profile $\widetilde{\mu}(r)$. We then add the $\widetilde{\mu}_{res}(r)$ profile to the analytical form of the best fit (i.e. the PSF-deconvolved model) and obtain a corrected profile $\widetilde{\mu}_{corr}(r)$, that is effectively deconvolved for the PSF [at least to first order, since the residual profile $\widetilde{\mu}_{res}(r)$ remains PSF-convolved]. Finally, we perform an analytical single Sérsic fit on these $\widetilde{\mu}_{corr}(r)$ profiles to obtain structural parameters that are corrected for PSF effects. Using our median-stacked profiles $\widetilde{\mu}(r)$ (both J_{F125W} and H_{F160W}; see Fig. 4), we find that for each galaxy population (both epochs), the effect of the PSF correction on our structural parameters is minimal. The effect on both r_e and n is typically < 1 per cent, and always < 3 per cent, even for compact galaxy populations (e.g. PSBs). Given that these differences are smaller than the stacking errors in our fitted structural parameters (see Table 2), we conclude that PSF effects have no significant impact on the results of this study. For a similar assessment of our optical profiles, see Section 6.

Another important consideration is the robustness of our $\widetilde{\mu}(r)$ profiles, and their fitted structural parameters (r_e, n), to the error in the sky subtraction (see Section 3.2). To address this issue, we use the following Monte Carlo analysis for both our J_{F125W} and H_{F160W} $\widetilde{\mu}(r)$ profiles. For each galaxy population, we generate 100 median-stacked profiles $\widetilde{\mu}_{sim}(r)$ using the same procedure as in Section 3.4, but with random sky offsets applied to each of the individual profiles. These offsets are generated by randomly sampling a Gaussian distribution with a standard deviation equal to the typical 1σ error in the sky subtraction $\widetilde{\sigma}_{sky}$ (see Section 3.2). The robustness of our results to the sky subtraction error is then determined from the variance between profile fits performed on these $\widetilde{\mu}_{sim}(r)$ profiles. For each galaxy population, we find that the effect of the sky subtraction error is minimal, with the effect on both

r_e and n typically < 5 per cent (for both J_{F125W} and H_{F160W}). We note that the differences observed in the structural parameters of our $\widetilde{\mu}(r)$ profiles (see Fig. 6) are robust to uncertainties at this level. Therefore, we conclude that errors in the sky subtraction have no significant effect on the results for our near-infrared $\widetilde{\mu}(r)$ profiles.

Finally, we note that in this study, the use of the stacked one-dimensional radial $\mu(r)$ profiles could also introduce some uncertainty to the fitted structural parameters due to the loss of azimuthal information, and an alternative would be to use two-dimensional analyses (i.e. stack galaxy images; see Section 3). However, the difference in structural parameters obtained from these two methods should be minimal, with a scatter at the 10–20 per cent level (see e.g. de Jong 1996; MacArthur et al. 2003; McDonald et al. 2011). We confirm this expected consistency by comparing the structural properties (r_e, n) from our individual galaxy $\mu(r)$ profiles (determined from our profile fitting method; see Section 4), with those obtained for the same galaxies in van der Wel et al. (2012). This work used two-dimensional Sérsic models (via GALFIT; Peng et al. 2002) to measure the near-infrared (J_{F125W} and H_{F160W}) structural properties of galaxies in CANDELS–UDS. As expected, for both J_{F125W} and H_{F160W}, we find good agreement between the structural properties determined from the two fitting methods, with a characteristic scatter (σ_{MAD}) at the 10–20 per cent level (typically < 10 per cent for r_e and < 20 per cent for n). We note that the differences observed in the structural properties of our $\widetilde{\mu}(r)$ profiles (see Fig. 6) are robust to uncertainties at this level.

4.3 Individual light $\mu(r)$ profiles

In this study, the median-stacked profiles $\widetilde{\mu}(r)$ are the principal focus, providing well-constrained typical structural properties for our galaxy populations (see Section 4.1). However, the Sérsic fits for our individual galaxy $\mu(r)$ profiles, despite having greater uncertainty due to the lower signal-to-noise, can also provide insight into the nature of our galaxy populations. The resultant structural properties (r_e, n) for our J_{F125W} and H_{F160W} individual $\mu(r)$ profiles are presented in Fig. 7. In all cases, we find that the median structural properties are very similar to those obtained from our $\widetilde{\mu}(r)$ profiles, with the same trends observed between the different galaxy populations (compare to Fig. 6). Similar trends in the structural properties are also observed in both the J_{F125W} and H_{F160W} wavebands. Furthermore, repeating these analyses using the physical effective radius r_e(kpc), as determined using the photometric redshift for each galaxy, produces analogous distributions and trends in the structural parameters. The median r_e(kpc) from these fits also confirm the physical r_e(kpc) determined for each galaxy population from our $\widetilde{\mu}(r)$ profiles (see Section 4.1). Furthermore, as with our $\widetilde{\mu}(r)$ profiles, we find PSF-effects and sky subtraction errors ($\pm\widetilde{\sigma}_{sky}$) to have a minimal influence on these individual fits, with a typical impact on the structural parameters (both r_e and n) of < 5 per cent and < 10 per cent, respectively.

With respect to these individual fits, we note that in some cases the profile fits have run into constraints caused by limitations in the model grid (e.g. at $n = 0.7$). These cases are rare in the passive and PSB populations (< 5 per cent), but more significant in the star-forming population (∼ 20 per cent). For these galaxies, the GALFIT structural parameters from van der Wel et al. (2012) suggest that the true Sérsic index is actually $\sim 0.7 \pm 0.1$ in most cases. Consequently, we retain these fits in our median analysis. However, we note that removing these cases only affects the median Sérsic index n for the star-forming galaxies at $1 < z < 2$ ($n \sim 1.3 \rightarrow 1.8$), and the overall trends in the structural parameters remain unaffected.

In addition to the median properties, these individual fits can also provide some further insight into the nature of rare subpopulations. For example, we find that the rare, high-mass PSBs at $z < 1$ ($M_* > 10^{10}\,M_\odot$; see Fig. 1) have structures which are similar to PSBs at $z > 1$, exhibiting analogous high n but also slightly larger r_e ($r_e > 2$ kpc). We shall return to this result in Section 7.2.

In conclusion, these individual $\mu(r)$ profile fits support our findings that PSBs at $z > 1$ are extremely compact and spheroidal [$r_e \sim 0.14$ arcsec (∼ 1.2 kpc), $n \sim 3.5$], while PSBs at $z < 1$ are generally compact but with more disc-like structures [$r_e \sim 0.24$ arcsec (∼ 1.5 kpc), $n \sim 1.8$]. Furthermore, the consistency between these results and those from our median-stacked $\widetilde{\mu}(r)$ profiles (see Section 4.1), confirms the effectiveness of our stacking analysis and demonstrates that our $\widetilde{\mu}(r)$ profiles are truly representative of their respective galaxy populations.

5 TWO-COMPONENT FITS

To explore the nature of PSBs in more detail, we extend our morphological analyses to allow for $\mu(r)$ profiles containing multiple components. Such analyses complement our single Sérsic fits, and provide further insight into the potential evolutionary histories of these galaxies. For example, for high-z PSBs we can investigate i) whether their stellar distributions are really compact, or if this is due to the point source emission from either an AGN or unresolved decaying nuclear starburst; and ii) whether these galaxies are genuinely spheroidally dominated, or if a bulge–disc system could equally account for their $\mu(r)$ profiles. To address these issues, two models will be considered: i) a Sérsic profile with a central point source (see Section 5.1); and ii) a bulge–disc system comprising a de Vaucouleurs (1959) bulge plus an exponential disc (see Section 5.2). For these fits, our stacking analysis is particularly important, enabling us to maximise signal-to-noise, particularly for the outer galactic regions. This is necessary for the identification of faint components (e.g. faint outer discs) that may not be detected in our individual profiles.

5.1 Sérsic profile + point source

In this work, we find PSBs to be extremely compact, particularly at $z > 1$ (see Figs. 6 and 7). One potential explanation is that these PSBs contain significant point source emission, from either an AGN or unresolved decaying nuclear starburst. This scenario would result in a $\mu(r)$ profile that would be inadequately modelled by a single Sérsic profile, and structural parameters biased towards low effective radii r_e and high Sérsic index n. Considering PSBs are recently quenched, the presence of an AGN might actually be expected (see e.g. Hopkins 2012), and may cause their host galaxies to appear compact. Alternatively, a decaying nuclear starburst may also be expected in PSBs, since many quenching processes are expected to result in gas being funnelled into the central regions of the galaxy. This could potentially trigger a nuclear starburst, and lead to a central concentration in the stellar distribution of the quenched system.

To address this issue, we include point source emission in our profile-fitting model, and assess the effect on the structure (r_e, n) of our galaxy populations. For profile fitting, the point source is modelled using the $\mu(r)$ profile of the relevant PSF (see Section 3.3), and added to the Sérsic profiles of the model library $\{\mu_{mock}(r)\}$ (see Section 4). To account for varying strengths of point source emission, we use more than 100 variations per model profile, with

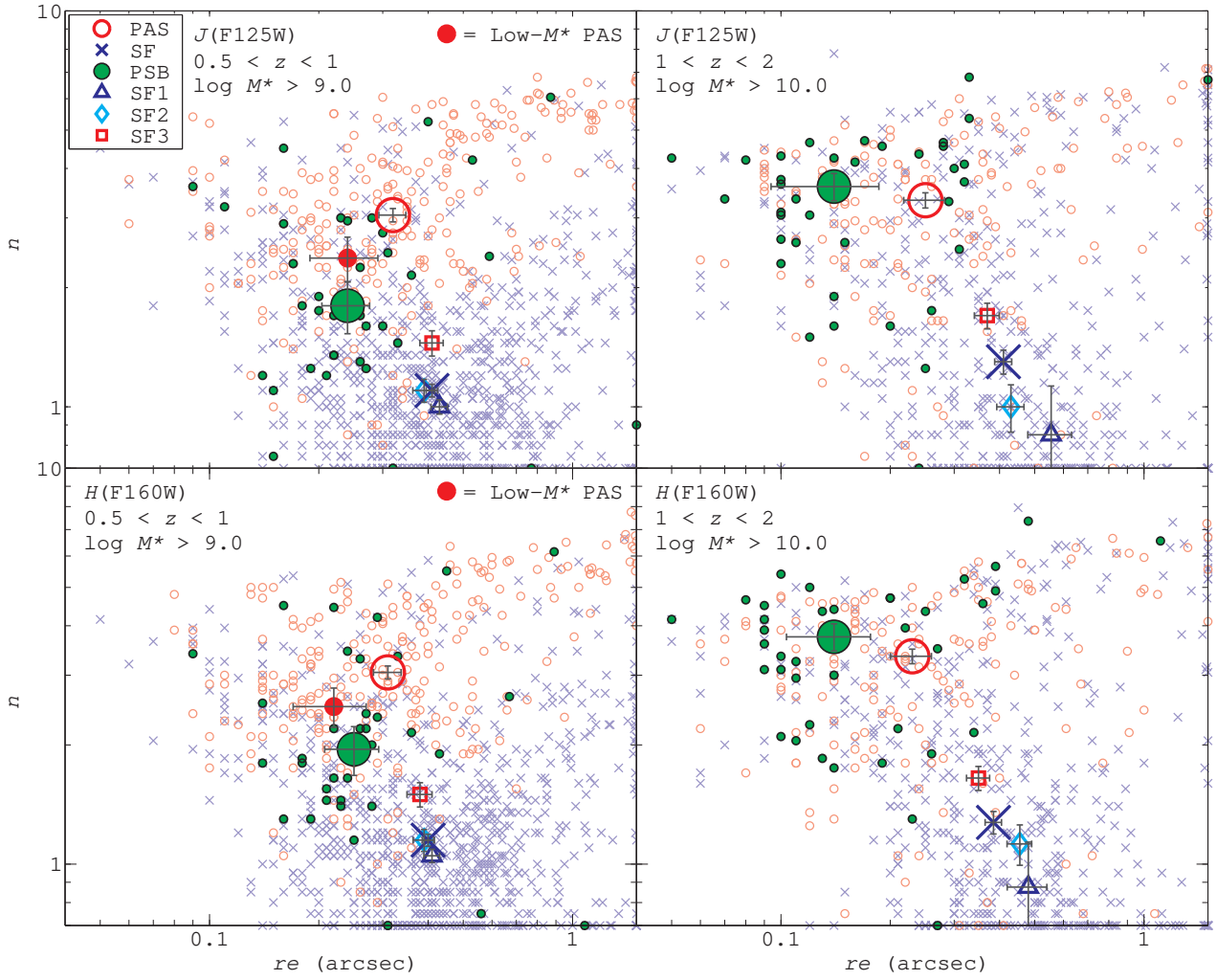

Figure 7. Structural properties (effective radius r_e, Sérsic index n) from the single Sérsic fits to our individual J_{F125W} (top row) and H_{F160W} (bottom row) $\mu(r)$ profiles. Results are shown for the passive (PAS), star-forming (SF) and PSB populations at two epochs: $0.5 < z < 1$ (left-hand panels) and $1 < z < 2$ (right-hand panels). Large symbols represent the median structural properties for each population, with associated 1σ errors. Median structural properties for the star-forming sub-populations (SF1 $\rightarrow$ SF3; based on decreasing sSFR) and the low-mass passive population ($10^9 < M_* < 10^{10}\,M_\odot$), are also shown. In all cases, the median structural properties are very similar to those obtained from our $\widetilde{\mu}(r)$ profiles, with the same trends observed between the different galaxy populations (compare to Fig. 6). These results support our findings that i) PSBs at $z > 1$ are extremely compact and spheroidal [$r_e \sim 0.14$ arcsec (~ 1.2 kpc), $n \sim 3.5$], with structures similar to massive passive galaxies but more compact; and ii) PSBs at $z < 1$ are also compact but with low n [$r_e \sim 0.24$ arcsec (~ 1.5 kpc), $n \sim 1.8$], and have structures similar to the low-mass passive population.

Table 3. Near-infrared Sérsic + point source fits: the structural properties for the Sérsic component of our median-stacked J_{F125W} and H_{F160W} light profiles $\widetilde{\mu}(r)$. Structural properties (r_e, n) are shown for different galaxy populations (passive, star-forming, PSB) at two different epochs, $0.5 < z < 1$ and $1 < z < 2$. Errors in the structural parameters (1σ) are determined from the variance between fits performed on 100 simulated $\widetilde{\mu}(r)$ profile stacks generated via a bootstrap method. For details of the corresponding point source component, see Table 4.

Galaxy Population	$0.5 < z < 1$				$1 < z < 2$			
	J_{F125W}		H_{F160W}		J_{F125W}		H_{F160W}	
	n	r_e (arcsec)	n	r_e (arcsec)	n	r_e (arcsec)	n	r_e (arcsec)
Passive	2.50 ± 0.19	0.32 ± 0.01	2.45 ± 0.19	0.31 ± 0.01	2.70 ± 0.29	0.23 ± 0.02	2.65 ± 0.26	0.23 ± 0.02
Star-forming	1.25 ± 0.06	0.39 ± 0.01	1.30 ± 0.05	0.38 ± 0.01	1.60 ± 0.10	0.38 ± 0.01	1.50 ± 0.08	0.36 ± 0.01
SF1	1.10 ± 0.05	0.40 ± 0.01	1.10 ± 0.05	0.39 ± 0.01	1.20 ± 0.16	0.52 ± 0.06	1.20 ± 0.15	0.47 ± 0.06
SF2	1.35 ± 0.08	0.39 ± 0.02	1.30 ± 0.08	0.38 ± 0.02	1.45 ± 0.13	0.43 ± 0.02	1.30 ± 0.11	0.41 ± 0.02
SF3	1.50 ± 0.15	0.39 ± 0.02	1.70 ± 0.14	0.36 ± 0.02	1.70 ± 0.12	0.34 ± 0.01	1.60 ± 0.12	0.32 ± 0.01
Post-starburst	1.55 ± 0.29	0.23 ± 0.02	1.55 ± 0.27	0.24 ± 0.01	3.50 ± 0.45	0.14 ± 0.02	2.55 ± 0.46	0.15 ± 0.03

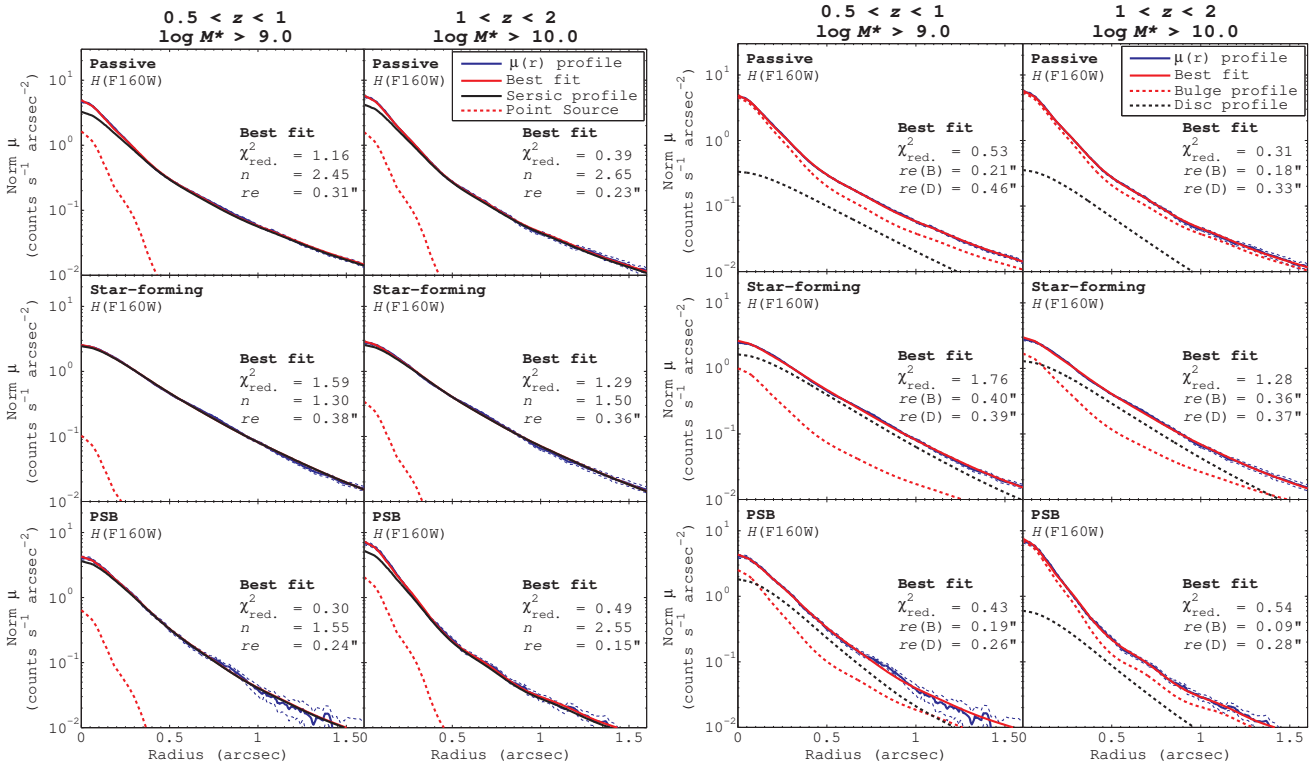

Figure 8. Two-component fits to our median-stacked $H_{\rm F160W}$ light profiles $\widetilde{\mu}(r)$. Left-hand panels: best-fits using a model comprising a Sérsic profile + point source. These fits show the *maximal* point source contribution, which is relatively minor for all populations (see also Fig. 9). Right-hand panels: best-fits using a model comprising a de Vaucouleurs ($r^{1/4}$) bulge + exponential disc. These fits yield the *maximal* likely bulge contribution, and show that at both epochs, passive galaxies are bulge-dominated, while star-forming galaxies are disc-dominated. In contrast, PSBs exhibit significantly different structures at different epochs: bulge-dominated at $1 < z < 2$, but disc-dominated at $0.5 < z < 1$.

point source emission accounting for between 0–100 per cent of the peak/central flux. Each model $\mu(r)$ profile (> 2000 000 in total) is then compared with the measured $\mu(r)$ profile and a χ^2 minimisation used to obtain the best fit. Note that since our $\widetilde{\mu}(r)$ profiles are already well-defined by a single Sérsic profile (see Fig. 5), the addition of a point source will not significantly improve the quality of the fit. Therefore, these fits are not intended to yield the actual point source contribution, but the *maximal* likely contribution to the $\mu(r)$ profile. The resultant best-fits for the $H_{\rm F160W}$ $\widetilde{\mu}(r)$ profiles are presented in Fig. 8. These profiles show that for all galaxy populations (both epochs), the *maximal* point source contribution is relatively minor and has little effect on their structural properties.

For each galaxy population, we determine the *maximal* point source contribution to the total light emitted by the galaxy (Pt/T). We compare these Pt/T measurements for the $J_{\rm F125W}$ and $H_{\rm F160W}$ $\widetilde{\mu}(r)$ profiles in Fig. 9. These results show that for all galaxy populations, typically < 15 per cent of the total light emitted can be attributed to a potential point source. Consequently, point source emission is not a major component in our $\widetilde{\mu}(r)$ profiles. The Pt/T for both the $J_{\rm F125W}$ and $H_{\rm F160W}$ $\widetilde{\mu}(r)$ profiles are presented in Table 4, with 1σ errors determined from a similar bootstrap analysis to that used for our single Sérsic fits (see Section 4.1). Furthermore, using a similar analysis to that described in Section 4.2, we find these measurements to be robust to sky subtraction errors ($\pm\widetilde{\sigma}_{\rm sky}$), with typical effects on Pt/T of < 10 per cent.

With respect to the Sérsic component, the resultant structural parameters ($r_{\rm e}$, n) are presented in Table 3. For each galaxy population, these are very similar to those produced by our single Sérsic fits (see Table 2), with the effective radius $r_{\rm e}$ being relatively unchanged and the Sérsic index n only decreasing slightly by the inclusion of a point source. The decrease in n is notably the strongest where the point source contribution is the most significant, i.e. passive galaxies and high-z PSBs (see Figs. 8 and 9). However, the differences between the structural properties of each galaxy population which are observed in our single Sérsic fits, all remain present (see Fig. 6). High-z PSBs ($z > 1$) remain compact [$r_{\rm e} \sim 0.15$ arcsec (~ 1.2 kpc)] and of relatively high Sérsic index ($n > 2.5$), even when the maximal contribution from a point source is taken into account. These PSBs also remain considerably more compact than the passive population. Consequently, point source emission, from either an AGN or unresolved decaying nuclear starburst, is not sufficient to explain the compact nature of massive PSBs at this epoch.

For our individual $\mu(r)$ profiles, we also perform analogous two-component fits. We note that these fits have greater uncertainty than those for our $\widetilde{\mu}(r)$ profiles, due to the lower signal-to-noise. Nonetheless, they may offer further insight into the nature of our galaxy populations. The resultant distributions of Pt/T in both $J_{\rm F125W}$ and $H_{\rm F160W}$, are presented in Fig. 9. In general, we find the same trends in the Pt/T of the galaxy populations as observed for our $\widetilde{\mu}(r)$ profiles. For both epochs, Pt/T is generally more significant in the passive population ($Pt/T_{\rm median} \sim 0.1$) than the star-forming population ($Pt/T_{\rm median} < 0.05$). This may indicate either an AGN or decaying nuclear starburst in a significant fraction of passive galaxies at these epochs (see also Whitaker et al. 2013, who report similar findings for passive galaxies at $z > 1.4$). For PSBs at both epochs, the Pt/T is generally low ($Pt/T_{\rm median} < 0.15$). However, we also find that at $1 < z < 2$ there is a population of PSBs that show evidence for a moderate *maximal* point source contribution

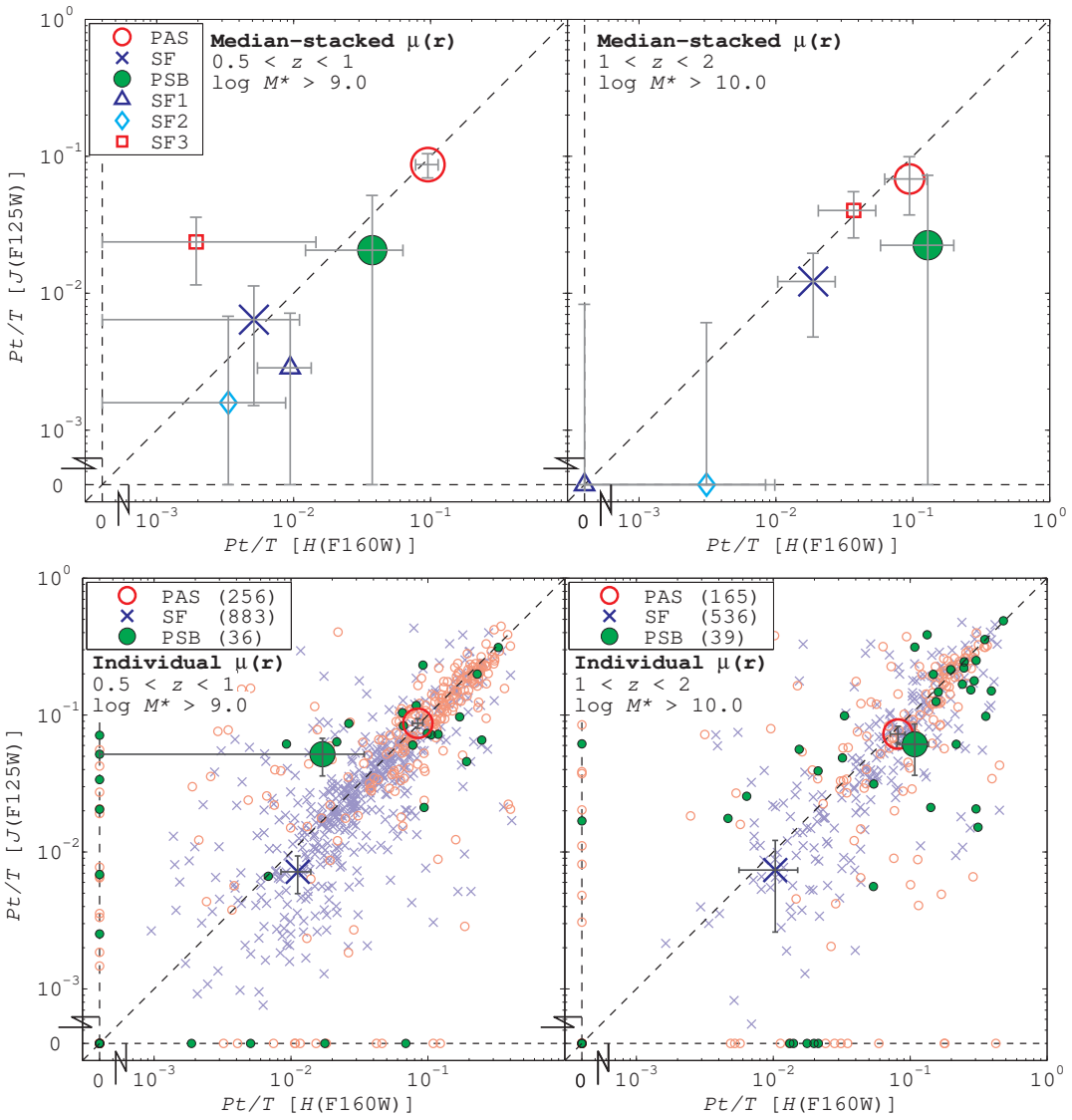

Figure 9. The *maximal* point source emission for our galaxy populations at two epochs: $0.5 < z < 1$ (left-hand panels) and $1 < z < 2$ (right-hand panels). A comparison of the maximal point source contribution (Pt/T) in $J_{\rm F125W}$ and $H_{\rm F160W}$ for the median-stacked light profiles $\widetilde{\mu}(r)$ (top panels), and for our individual $\mu(r)$ profiles (bottom panels). In the bottom panels, large symbols represent the median Pt/T in each population, with associated 1σ errors in the median position. For each population, typically < 15 per cent of the total light emitted can be attributed to a potential point source.

Table 4. Near-infrared multiple component fits: the *maximal* contribution of point-source/bulge light to the total light from the galaxy (Pt/T and B/T, respectively) for our median-stacked $J_{\rm F125W}$ and $H_{\rm F160W}$ light profiles $\widetilde{\mu}(r)$. Results are shown for different galaxy populations (passive, star-forming, PSB) at two different epochs, $0.5 < z < 1$ and $1 < z < 2$. Errors in these measurements (1σ) are determined from the variance between fits performed on 100 simulated $\widetilde{\mu}(r)$ profile stacks generated via a bootstrap method.

Galaxy Population	$0.5 < z < 1$				$1 < z < 2$			
	$J_{\rm F125W}$		$H_{\rm F160W}$		$J_{\rm F125W}$		$H_{\rm F160W}$	
	Pt/T ($\times 10^{-2}$)	B/T	Pt/T ($\times 10^{-2}$)	B/T	Pt/T ($\times 10^{-2}$)	B/T	Pt/T ($\times 10^{-2}$)	B/T
Passive	8.70 ± 1.75	0.78 ± 0.04	9.56 ± 1.79	0.76 ± 0.04	6.83 ± 3.10	0.83 ± 0.04	9.46 ± 3.23	0.84 ± 0.04
Star-forming	0.64 ± 0.49	0.19 ± 0.03	0.51 ± 0.59	0.21 ± 0.02	1.22 ± 0.74	0.41 ± 0.04	1.87 ± 0.84	0.36 ± 0.03
SF1	0.29 ± 0.43	0.07 ± 0.03	0.94 ± 0.40	0.10 ± 0.03	0.00 ± 0.79	0.15 ± 0.09	0.00 ± 0.80	0.15 ± 0.09
SF2	0.16 ± 0.52	0.24 ± 0.04	0.33 ± 0.54	0.22 ± 0.04	0.00 ± 0.57	0.31 ± 0.07	0.31 ± 0.67	0.28 ± 0.06
SF3	2.37 ± 1.22	0.37 ± 0.07	0.19 ± 1.26	0.42 ± 0.06	4.02 ± 1.49	0.48 ± 0.05	3.70 ± 1.66	0.45 ± 0.05
Post-starburst	2.06 ± 3.12	0.40 ± 0.12	3.75 ± 2.53	0.40 ± 0.12	2.24 ± 5.02	0.90 ± 0.07	12.86 ± 7.05	0.77 ± 0.08

($Pt/T > 0.1$; ~ 40 per cent), and that these cases are much rarer at $0.5 < z < 1$ ($Pt/T > 0.1$; ~ 15 per cent). Taken together, these results indicate that while in general, point source emission is not driving the compact nature of PSBs, at high redshift ($z > 1$) we cannot rule out that a fraction of these galaxies may host either an AGN or unresolved decaying nuclear starburst. These results also suggest that PSBs at $z > 1$ may have experienced a different evolutionary history to those at lower redshifts.

5.2 Bulge–disc decomposition

In this work, we find a significant difference in the structure of PSBs at different epochs (see Figs. 6 and 7). PSBs at $z > 1$ are typically massive ($M_* > 10^{10}\,M_\odot$), very compact and of high n; while at $z < 1$, they are generally of lower mass ($M_* < 10^{10}\,M_\odot$) and exhibit compact but less concentrated profiles (i.e. lower n). This suggests that PSBs at $z > 1$ are typically spheroidal systems, while at $z < 1$ they contain a significant stellar disc. However, although Sérsic index n is generally considered a good proxy for bulge–disc structure, recent works have shown that this is not necessarily the case (e.g. Bruce et al. 2014). Furthermore, since single Sérsic fits are largely driven by the central regions of the profile, the presence of a faint outer disc can easily be missed. Therefore, to investigate the structure of these galaxies in more detail, we perform bulge–disc (B–D) decomposition and assess the contribution of these two main structural components to the overall structure.

To perform B–D decomposition, we use a two-component model comprising a de Vaucouleurs ($r^{1/4}$) bulge and single exponential disc. The motivation behind adopting this bulge profile, instead of the more realistic free Sérsic profile, is to i) avoid the degeneracy and instability issues inherent to adding more degrees of freedom to the models; and ii) restrict the range of parameter space that needs to be explored in the fitting. We note that in adopting this bulge profile, we do not necessarily obtain its actual contribution, and that many of our galaxies will have less concentrated bulges (i.e. pseudo-bulges), particularly at low-mass ($M_* < 10^{10}\,M_\odot$; see e.g. Fisher & Drory 2011). Therefore, by design these fits will not yield the actual bulge components, but the *maximal* likely bulge contribution. For profile fitting, the sum of a wide range of bulge and disc profiles are compared to the measured $\mu(r)$ profile and a χ^2 minimisation used to find the best fit. In this process, the Sérsic index of the bulge and disc are fixed at $n = 4$ and $n = 1$, respectively, but the effective radius r_e and normalisation of each component are free to vary. For both components, the full r_e parameter space probed by the model library is analysed, ensuring a global minimum solution is obtained.

For each population, the resultant best-fits for the H_{F160W} $\widetilde{\mu}(r)$ profiles are presented in Fig. 8. In all cases, we find the $\widetilde{\mu}(r)$ profile to be well-described by a B–D system (i.e. $\chi^2_{red} \sim 1$). However, since these profiles are already well-described by a single Sérsic profile (see Fig. 5), the adoption of a B–D model does not necessarily improve the quality of the fit. Therefore, it is important to note that these B–D decompositions only yield the most likely structure, assuming a two-component B–D system. A comparison of the J_{F125W} and H_{F160W} bulge-to-total light ratios (B/T) is presented in Fig. 10 and Table 4. The 1σ errors in B/T are determined using a similar bootstrap analysis to that used for our single Sérsic fits (see Section 4.1). Furthermore, using a similar analysis to that described in Section 4.2, we find these measurements to be robust to sky subtraction errors ($\pm\widetilde{\sigma}_{sky}$), with typical effects of < 10 per cent. For passive and star-forming galaxies, we find similar results at both epochs ($0.5 < z < 1$ and $1 < z < 2$), with the passive population being bulge-dominated ($B/T \sim 0.8$) and the star-forming populations being generally disc-dominated ($B/T < 0.5$). For the star-forming sub-populations (SF1–3), we find that at both epochs, all are relatively disc-dominated but there is an increase in B/T from SF1 $\rightarrow$ SF3 (i.e. with increasing mean stellar age). Interestingly, for PSBs we observe a significant difference in B/T at different epochs. At $z > 1$, the PSBs exhibit bulge-dominated profiles ($B/T \sim 0.8$), and with B–D structures similar to the massive passive population. It is also clear from Fig. 8, that these galaxies contain no significant faint outer disc. In contrast at $z < 1$, PSBs have completely different structures with much more significant disc components ($B/T \sim 0.4$), and with B–D structures not dissimilar to those of the low-mass passive population ($M_* < 10^{10}\,M_\odot$).

For our individual $\mu(r)$ profiles, we also perform analogous B–D decompositions. We note that these fits have much greater uncertainty than those for the $\widetilde{\mu}(r)$ profiles, but nonetheless can still provide insight into the nature of our galaxy populations. The resultant B/T distributions in both J_{F125W} and H_{F160W}, are presented in Fig. 10. In general, although there is significant scatter, we find similar results as before for our $\widetilde{\mu}(r)$ profiles, with PSBs having bulge-dominated profiles at $z > 1$, and more significant disc components at $z < 1$.

With respect to these results, recall that our B–D decompositions yield the *maximal* bulge contribution and consequently will likely overestimate this component, especially at low masses ($M_* < 10^{10}\,M_\odot$; see e.g. Fisher & Drory 2011). This is particularly relevant for PSBs at $z < 1$, which will be even more disc-dominated than our results suggest, but less of an issue at $z > 1$. We therefore conclude that there is a significant difference in the B–D structure of PSBs at different epochs, which suggests that PSBs at $z > 1$ have undergone a completely different evolutionary history compared to their counterparts at lower redshifts.

6 OPTICAL IMAGING

In this paper, we mainly focus on the structural analyses for our near-infrared $\mu(r)$ profiles. At the redshifts studied here ($0.5 < z < 2$), these profiles generally trace the distribution of the old stellar component (i.e. $\lambda_{rest} > 4000$ Å), which comprises the bulk of the stellar mass. However, an important addition to this study is the structural analyses for our optical $\mu(r)$ profiles (V_{F606W}, I_{F814W}), which can be used to probe the distribution of younger, more recently formed stellar populations (i.e. O B A F stars; see later discussion for further details). Such analyses can be used to determine whether these younger stars trace the stellar mass, or whether they are more centrally located, which for PSBs can place useful constraints on their evolutionary history (e.g. whether the preceding starburst was strongly centralized). These structural analyses are analogous to those presented for our near-infrared profiles in Section 4. However, since our optical profiles are generally of poorer quality than those in the near-infrared (i.e. fainter and with more significant noise), these structural analyses are limited to single Sérsic fits only.

For each galaxy population, the median stacked profiles $\widetilde{\mu}(r)$ from both the CANDELS V_{F606W} and I_{F814W} imaging are presented in Fig. 11. The V_{F606W} $\widetilde{\mu}(r)$ profiles are limited to the intermediate-z epoch ($0.5 < z < 1$), due to the inadequate signal-to-noise in this waveband at $z > 1$. As with our near-infrared profiles, we perform single Sérsic fits on these $\widetilde{\mu}(r)$ profiles, and obtain the typical structural properties (r_e, n) of each galaxy population (see Fig. 11 and Table 5). The 1σ errors in these structural parameters are determined from the variance between fits performed on

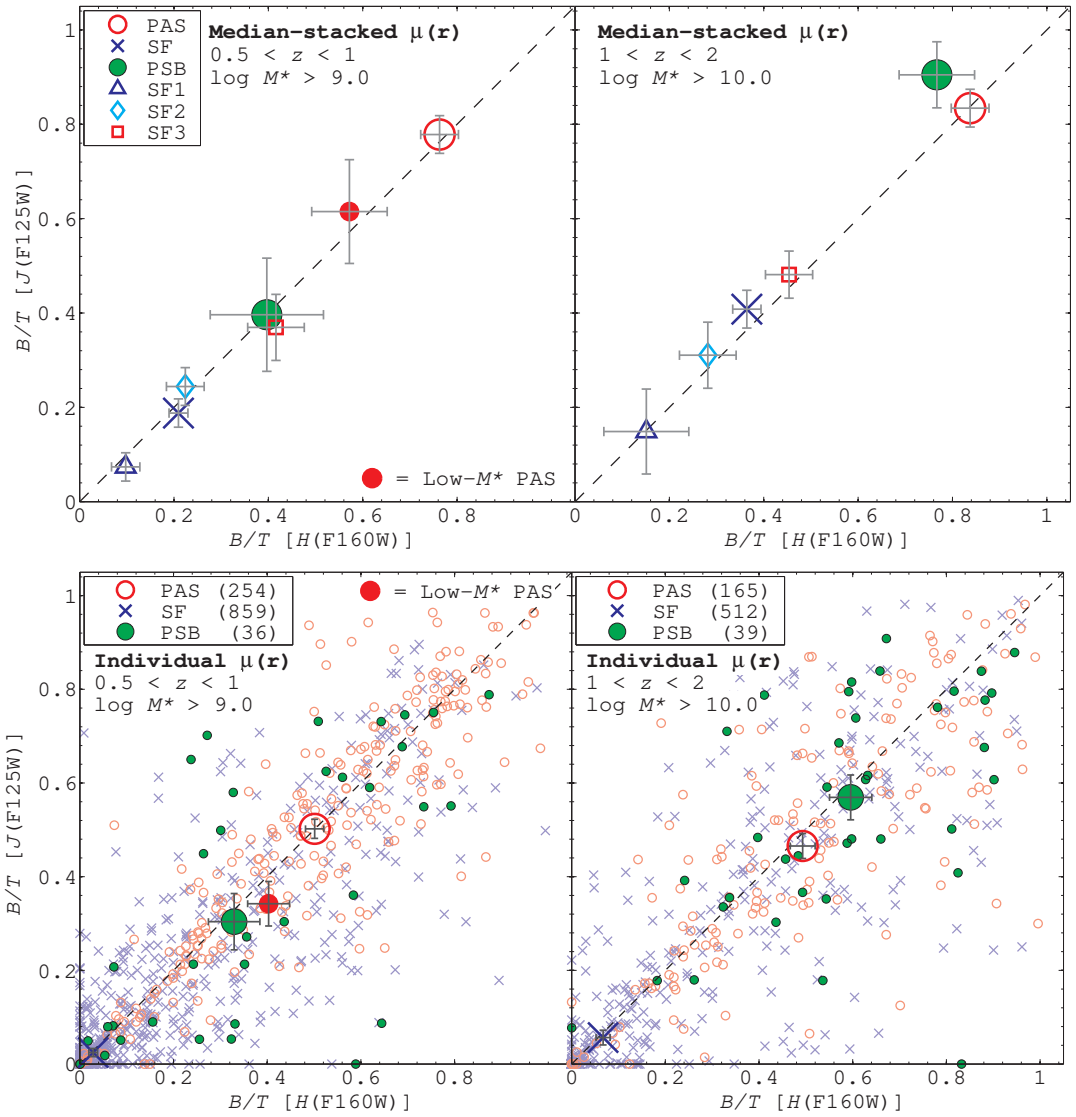

Figure 10. Bulge–disc (B–D) decompositions for our galaxy populations at two epochs: $0.5 < z < 1$ (left-hand panels) and $1 < z < 2$ (right-hand panels). A comparison of the *maximal* bulge-to-total ratio (B/T) in $J_{\rm F125W}$ and $H_{\rm F160W}$ for the median-stacked light profiles $\widetilde{\mu}(r)$ (top panels), and for our individual $\mu(r)$ profiles (bottom panels). In the bottom panels, large symbols represent the median B/T in each population, with associated 1σ errors. The typical B/T for the low-mass passive population ($10^9 < M_* < 10^{10}\,{\rm M}_\odot$) is also indicated. We find PSBs to exhibit significantly different structures at different epochs: bulge-dominated at $1 < z < 2$, but disc-dominated at $0.5 < z < 1$.

Table 5. Optical single Sérsic fits: the structural properties for our median-stacked $V_{\rm F606W}$ and $I_{\rm F814W}$ light profiles $\widetilde{\mu}(r)$. Structural properties ($r_{\rm e}$, n) are shown for different galaxy populations (passive, star-forming, PSB) at two different epochs, $0.5 < z < 1$ and $1 < z < 2$. Errors in the structural parameters (1σ) are determined from the variance between fits performed on 100 simulated $\widetilde{\mu}(r)$ profile stacks generated via a bootstrap method.

Galaxy Population	$0.5 < z < 1$				$1 < z < 2$			
	$V_{\rm F606W}$		$I_{\rm F814W}$		$V_{\rm F606W}$		$I_{\rm F814W}$	
	n	$r_{\rm e}$ (arcsec)	n	$r_{\rm e}$ (arcsec)	n	$r_{\rm e}$ (arcsec)	n	$r_{\rm e}$ (arcsec)
Passive	3.75 ± 0.24	0.41 ± 0.03	3.60 ± 0.20	0.32 ± 0.02	-	-	4.05 ± 0.33	0.27 ± 0.03
Star-forming	1.75 ± 0.09	0.45 ± 0.02	1.45 ± 0.06	0.42 ± 0.02	-	-	2.80 ± 0.23	0.38 ± 0.04
SF1	1.60 ± 0.11	0.45 ± 0.03	1.25 ± 0.05	0.43 ± 0.02	-	-	2.25 ± 0.89	0.37 ± 0.23
SF2	1.65 ± 0.20	0.46 ± 0.04	1.40 ± 0.10	0.43 ± 0.03	-	-	2.65 ± 0.34	0.40 ± 0.06
SF3	2.20 ± 0.28	0.47 ± 0.04	1.95 ± 0.18	0.43 ± 0.04	-	-	3.45 ± 0.46	0.38 ± 0.05
Post-starburst	1.90 ± 0.63	0.23 ± 0.04	2.05 ± 0.31	0.20 ± 0.02	-	-	4.10 ± 0.62	0.15 ± 0.04

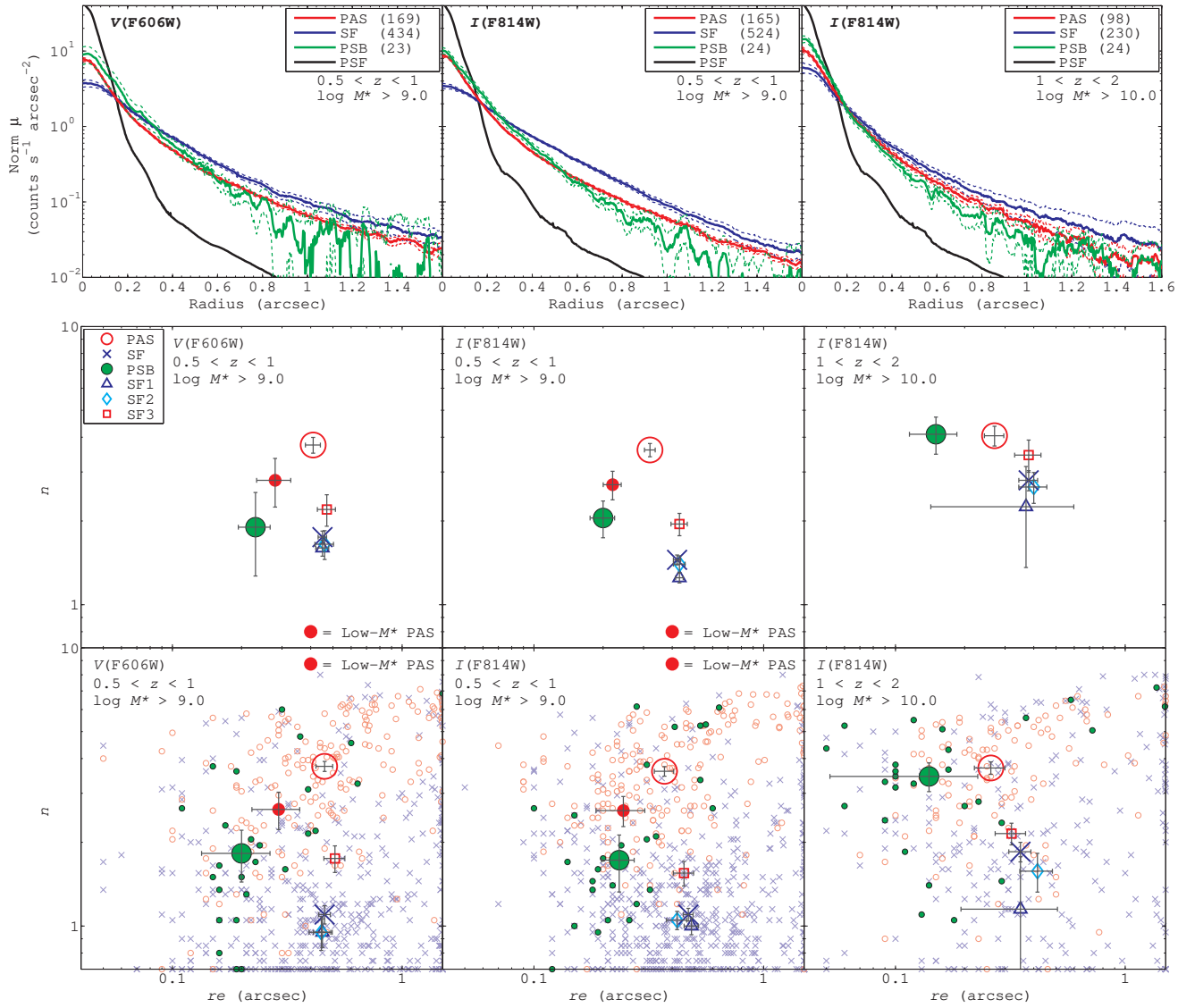

Figure 11. Structural analyses for our optical $\mu(r)$ profiles (ACS – $I_{\rm F814W}$, $V_{\rm F606W}$). Top row: median-stacked optical light profiles $\widetilde{\mu}(r)$ for different galaxy populations and at different epochs: $V_{\rm F606W}$ at $0.5 < z < 1$ (left-hand panel), $I_{\rm F814W}$ at $0.5 < z < 1$ (centre panel), and $I_{\rm F814W}$ at $1 < z < 2$ (right-hand panel). Middle row: the corresponding structural parameters ($r_{\rm e}$, n) from the single Sérsic fits to these optical $\widetilde{\mu}(r)$ profiles. Bottom row: structural parameters from corresponding analogous fits to the individual optical $\mu(r)$ profiles, with the large symbols showing the median structural properties of each population (including associated 1σ errors). The typical structural properties for the low-mass passive population ($10^9 < M_* < 10^{10}\,{\rm M}_\odot$) are also indicated. The results of these structural analyses are further summarised in Fig. 12, and compared to the corresponding results from our near-infrared $\mu(r)$ profiles.

100 simulated $\widetilde{\mu}(r)$ stacks generated via a bootstrap analysis. We also find that in all cases, the $\widetilde{\mu}(r)$ profiles are well described by a single Sérsic profile, with the best fit having a reduced chi-squared $\chi^2_{\rm red} \sim 1$. Analogous fits were also performed on the individual $\mu(r)$ profiles (see Fig. 11). Finally, as with our near-infrared profiles (see Section 4.2), we find PSF-effects and sky subtraction errors to have a minimal influence on both $r_{\rm e}$ and n (typically < 10 per cent). In the following, we compare the results of these fits to those obtained from the near-infrared wavebands in Section 4. A summary of these comparisons is presented in Fig. 12.

At high redshift ($1 < z < 2$), both passive and PSB galaxies show no significant variation in their structural properties between the optical ($I_{\rm F814W}$) and near-infrared wavebands (see Fig. 12). In both regimes, these populations exhibit compact and spheroidal structures; passive [$n \sim 3.5$, $r_{\rm e} \sim 0.25$ arcsec (~ 2.1 kpc)]; PSB [$n \sim 3.5$, $r_{\rm e} \sim 0.15$ arcsec (~ 1.3 kpc)]. In contrast, star-forming galaxies have significantly larger n in $I_{\rm F814W}$ compared to the near-infrared ($n_{\rm F814W} \sim 3$ vs. $n_{\rm near-IR} \sim 1.5$ from the $\widetilde{\mu}(r)$ profiles). Note that at these redshifts, $I_{\rm F814W}$ probes a different stellar population to the near-infrared (i.e. $\lambda_{\rm rest} < 4000$ Å), and generally traces younger stellar populations (O B A F stars). Therefore, these comparisons indicate that at $z > 1$: i) younger stars in passive/PSB galaxies trace the structure of the old stellar population (i.e. stellar mass), which for PSBs suggests that the preceding starburst and/or quenching was not strongly centralized and occurred throughout the stellar distribution; and ii) in star-forming galaxies, younger stars are more centralized than the old stellar population (i.e. more prominent in the central bulge, than the outer disc).

At intermediate redshift ($0.5 < z < 1$), for both star-forming and PSB galaxies, we also find no significant variation in structure between the optical ($I_{\rm F814W}$, $V_{\rm F606W}$) and near-infrared wavebands (see Fig. 12). Star-forming galaxies are extended and disc-like

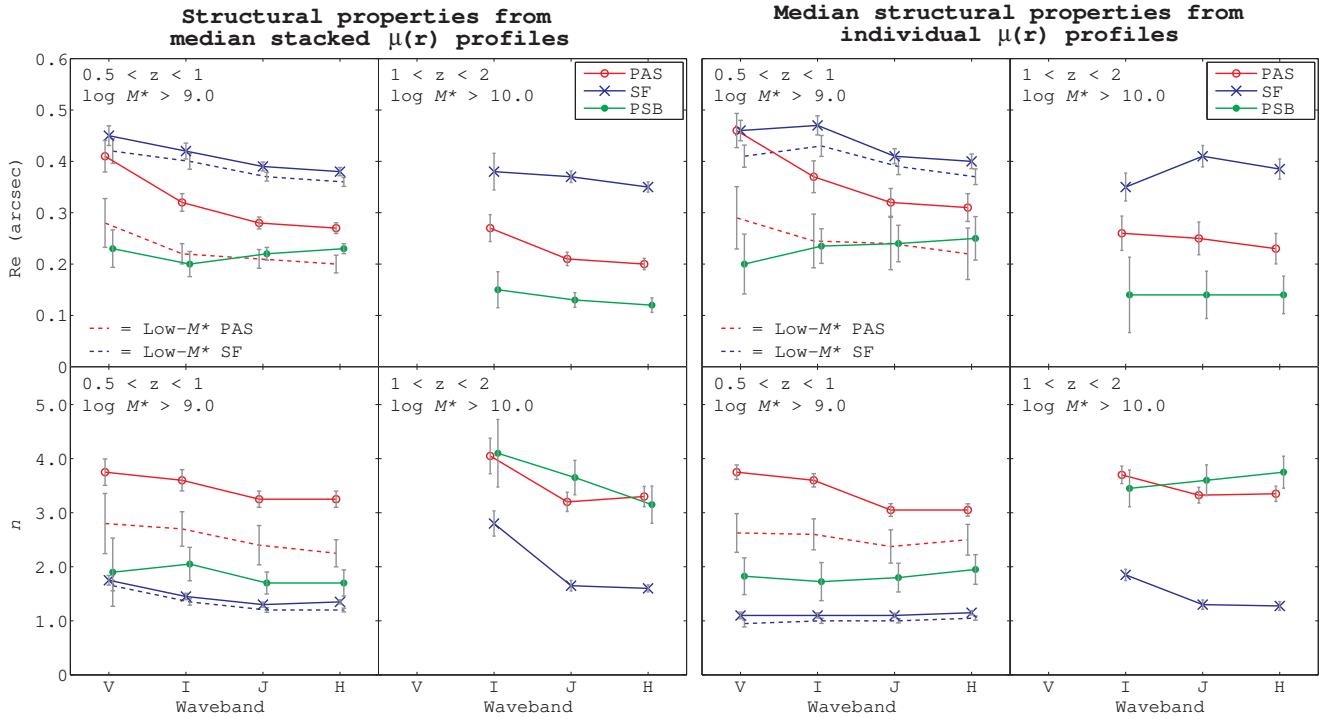

Figure 12. The wavelength dependence of structural parameters (r_e, n) for our galaxy populations at two epochs ($0.5 < z < 1$ and $1 < z < 2$). Left-hand panels: a summary of results from the single Sérsic fits to our median-stacked profiles $\widetilde{\mu}(r)$ across all four CANDELS wavebands ($V_{\rm F606W}$, $I_{\rm F814W}$, $J_{\rm F125W}$, $H_{\rm F160W}$). Right-hand panels: an analogous summary for the median structural properties (r_e, n) of our individual $\mu(r)$ profiles. Both the median-stacked $\widetilde{\mu}(r)$ and individual $\mu(r)$ profile analyses yield consistent results. For both epochs, PSBs show consistent structural parameters across all wavebands, regardless of whether the light being traced is dominated by the old stellar component ($\lambda_{\rm rest} > 4000$ Å) or younger stellar populations ($\lambda_{\rm rest} < 4000$ Å).

[$r_e \sim 0.45$ arcsec (~ 3.3 kpc), $1 < n < 2$], and PSBs are compact and of low n [$r_e \sim 0.2$ arcsec (~ 1.5 kpc), $n \sim 2$]. Furthermore, across all wavebands, PSBs have structures that are similar to the low-mass passive population, the population into which they will most likely evolve. Note that at this epoch, $I_{\rm F814W}$ will trace a similar stellar population as the near-infrared, but $V_{\rm F606W}$ will generally trace younger populations (i.e. $\lambda_{\rm rest} < 4000$ Å; O B A F stars). Therefore, these results indicate that at $0.5 < z < 1$, younger stars in star-forming/PSB galaxies trace the structure of the old stellar population (i.e. stellar mass). For PSBs, this again suggests that the preceding starburst and/or quenching was not strongly centralized (i.e. it was global in nature). In contrast, the general passive population exhibits significantly larger r_e in the optical wavebands compared to the near-infrared, especially in $V_{\rm F606W}$ ($\Delta r_e \sim 40$ per cent). Interestingly, this trend could indicate younger stars in the outskirts of passive galaxies at this epoch ($z < 1$). This might be expected if they were quenched from the 'inside–out' (see e.g. Tacchella et al. 2016), or if a minor merger resulted in the accretion of younger stars to an outer envelope (e.g. Naab et al. 2009).

Finally, we note that our conclusions above assume that the majority of light emitted at $\lambda_{\rm rest} < 4000$ Å originates from young stellar populations (O B A F stars). In order to quantify this for our PSBs we create simple mock spectra using Bruzual & Charlot (2003) models, assuming solar metallicity, Chabrier IMF, and a moderate amount of dust attenuation (effective attenuation $\tau_V = 1.0$ and fraction of dust in the interstellar medium $\mu = 0.3$, following the Charlot & Fall 2000 dust model as adapted by Wild et al. 2011). We assume two underlying star-formation histories, both 6 Gyr old and exponentially declining with a timescale of 0.1 or 3 Gyr, to represent an underlying quiescent or star-forming population. Superimposed on this is a 500 Myr old burst population, with an exponentially declining star-formation history of timescale 0.3 Gyr, and varying burst mass fraction. For a burst mass fraction of 10 per cent, the minimum expected for our photometrically-selected PSBs, we calculate the fraction of light from the burst population in both $V_{\rm F606W}$ and $H_{\rm F160W}$ at $z = 0.75$, and $I_{\rm F814W}$ and $H_{\rm F160W}$ at $z = 1.5$ (the central redshifts of the epochs studied). We find $\sim$ 70–80 per cent of the light in the optical wavebands is from the burst population, compared to $\sim$ 40 per cent in $H_{\rm F160W}$ for both epochs. Consequently, this shows that the optical/near-infrared wavebands used in this study are able to broadly differentiate between the young and old stellar populations in our PSB galaxies.

7 SUMMARY AND DISCUSSION

In this study, we have explored in detail the structure of PSBs at $0.5 < z < 2$. For this we have used a combination of near-infrared and optical $\mu(r)$ profiles, probing both the old stellar component as well as younger, and more recently formed stellar populations. Various structural analyses have also been performed, including single Sérsic and multiple component fits, which have revealed significant differences in the structure of PSBs at different epochs. At $z > 1$, PSBs are typically massive ($M_* > 10^{10}\,{\rm M}_\odot$), very compact and exhibit high Sérsic indices n, with structures that differ significantly from their star-forming progenitors, but are similar to massive passive galaxies. In contrast at lower redshift ($0.5 < z < 1$), PSBs are generally of low mass ($M_* < 10^{10}\,{\rm M}_\odot$) and exhibit compact but less concentrated profiles (i.e. lower n), with structures similar to low-mass passive galaxies (i.e. passive discs).

Taken together, these results suggest that PSBs at $z > 1$ are an intrinsically different population to those at $z < 1$, indicating

different quenching routes are active at different epochs, with the PSB phase being triggered by different processes. Furthermore, for both epochs, we find a remarkable consistency in PSB structure across the optical/near-infrared wavebands, which suggests that the old/intermediate–young aged stellar populations probed follow the same distribution. This implies that any preceding starburst and/or quenching in these galaxies was not strongly centralized, and therefore occurred globally. In this section, we present a more in depth discussion of these results and their implications for the potential quenching mechanisms experienced by PSBs at different epochs. To complement this discussion, we refer the reader to Fig. 12, which provides a summary of our structural analyses across each of the four CANDELS wavebands ($V_{\rm F606W}$, $I_{\rm F814W}$, $J_{\rm F125W}$, $H_{\rm F160W}$).

7.1 Post-starburst galaxies at $1 < z < 2$

For the high-redshift epoch ($1 < z < 2$), the main results from our structural analyses can be summarised as follows:

(i) PSBs at $z > 1$ are of high mass ($M_* > 10^{10}\,{\rm M}_\odot$), and exhibit structures that are extremely compact [$r_{\rm e} \sim 0.13$ arcsec, (~ 1.1 kpc)] and of high Sérsic index ($n \sim 3.5$). In general, their structures differ from those of their star-forming progenitors, and are more similar to those of the old massive passive population, although considerably more compact (by ~ 40 per cent). These results confirm the recent findings of Almaini et al. (2017), who find that massive PSBs at $z > 1$ are compact proto-spheroids. This implies that morphological/structural transformation must have occurred prior to the post-starburst phase, and therefore before (or during) the event that quenched the galaxy's star formation (see Sections 4.1 and 4.3).

(ii) Point source emission from either an AGN or unresolved decaying nuclear starburst is not sufficient to explain the compact nature of massive PSBs at this epoch. Even when the *maximal* emission from a potential point source is taken into account, these PSBs remain compact [$r_{\rm e} \sim 0.15$ arcsec, (~ 1.2 kpc)] and of relatively high Sérsic index ($n > 2.5$). They also remain significantly more compact than the massive passive population. However, we note that while point source emission cannot explain their compact nature, we cannot rule out the presence of an AGN, or unresolved decaying nuclear starburst in a fraction (< 40 per cent) of PSBs at this epoch (see Section 5.1).

(iii) Bulge–disc decomposition indicates that massive PSBs at $z > 1$ are generally bulge-dominated systems ($B/T \sim 0.8$), with little or no residual disc component. Their B/T is similar to those of the old massive passive population (see Section 5.2).

(iv) Massive PSBs at $z > 1$ exhibit consistent structural parameters ($r_{\rm e}$, n) between all three wavebands studied at this epoch (see Fig. 12). This consistency between wavebands probing both the old stellar component ($\lambda_{\rm rest} > 4000$ Å; $J_{\rm F125W}$ and $H_{\rm F160W}$) and younger populations (O B A F stars; $\lambda_{\rm rest} < 4000$ Å; $I_{\rm F814W}$) indicates that younger stars are tracing the old stellar population (i.e. stellar mass) in these galaxies. This suggests that any preceding starburst and/or quenching was not strongly centralized within the existing stellar distribution (i.e. it was global in nature). In contrast, massive star-forming galaxies show a significant increase in Sérsic index moving from the near-infrared to the optical wavebands (i.e. old $\rightarrow$ younger stellar populations), potentially indicating centralized star-formation in these galaxies and the build-up of galactic bulges at this epoch (see Fig. 12 and Section 6).

The results presented here suggest that high-z PSBs ($z > 1$) have experienced a major disruptive event that quenched their star formation and led to a 'compaction' of the stellar distribution. Such an event could be a gas-rich major merger (e.g. Hopkins et al. 2009; Wellons et al. 2015) or a dissipative 'protogalactic collapse': gas inflow to a massive disc, which then destabilises and collapses (e.g. Dekel et al. 2009; Zolotov et al. 2015). In both cases, gas would be driven into the central galactic regions, triggering a starburst, and lead to the formation of a compact remnant. We note that in our observations the lack of excess young (O B A F) stars in the central regions of PSBs does not necessarily rule out these scenarios (see later discussion, for more details). Following this 'compaction' event, any subsequent star formation would be rapidly quenched via feedback from either an AGN or the starburst itself, both of which would result in the characteristic post-starburst spectral features (i.e. strong Balmer absorption). These scenarios would also naturally lead to the destruction of the stellar disc and the formation of a compact spheroidally-dominated stellar distribution (i.e. high n and high B/T), both of which match our observations. Furthermore, since these scenarios lead to significant structural transformations during the quenching event, they are consistent with our findings that PSBs at this epoch already exhibit structures similar to the massive passive galaxies into which they will most likely evolve.

At low redshift ($z < 0.1$), gas-rich major mergers have also been linked to PSBs in low-density environments (e.g. Zabludoff et al. 1996; Blake et al. 2004; Pawlik et al. 2016, 2018). However, in contrast to our results at $z > 1$, several studies have reported centrally-concentrated young stellar populations in these galaxies (e.g. Norton et al. 2001; Yamauchi & Goto 2005; Pracy et al. 2013), indicative of a merger-induced centralized starburst. Despite these low redshift results, we note that the lack of a stellar-age gradient in our high-z PSBs does not necessarily rule out a gas-rich merger scenario for their origin, since the remnant structure will be strongly dependent on the nature of these mergers at high/low redshift. At low redshift, gas-rich mergers will funnel gas into the central regions of the galaxy and trigger a nucleated starburst prior to the PSB phase. In contrast, at $z > 1$ these events will be significantly more gas rich than their local counterparts, leading to a more substantial starburst and the formation of a compact remnant (see discussion above). This would potentially lead to either: i) the bulk of the stellar mass being formed during a centralized starburst (e.g. monolithic collapse); or ii) a compaction of the original structure to subsequently match that of the starburst itself. Both of these scenarios would result in little or no radial age gradient in the PSB phase, matching our observations.

In comparison to previous works, we find that our results confirm those of the recent study by Almaini et al. (2017), who also performed a detailed structural analysis of high-redshift PSBs ($z > 1$) in the UDS field. Using both ground-/space-based near-infrared imaging (UDS-K and CANDELS-$H_{\rm F160W}$), they use two-dimensional Sérsic models to examine the stellar structure of massive ($M_* > 10^{10}\,{\rm M}_\odot$) PSBs at $z > 1$. They also conclude that PSBs at this epoch are exceptionally compact and with structures similar to the old massive passive population (i.e. high Sérsic indices; spheroidally-dominated). Furthermore, they find evidence for massive PSBs being smaller on average than comparable passive galaxies at the same epoch, which is also consistent with our structural analyses (see Fig. 12). Similar results have also been reported at $z > 1$ by Whitaker et al. (2012) and Yano et al. (2016), where younger passive galaxies are found to be more compact than their older counterparts. However, we note that at more modest redshifts ($z \sim 1$) previous studies have found conflicting results on the relationship between stellar age and the compact-

ness of passive/recently-quenched galaxies (e.g. Keating et al. 2015; Williams et al. 2017), and further study is still required.

In conclusion, these results indicate that PSBs at high-redshift ($z > 1$) are quenched in a relatively violent event (e.g. a gas-rich major merger or protogalactic collapse), that led to a 'compaction' of the stellar distribution, and that this may be followed by a gradual growth in size as the galaxy evolves into a more established passive system (e.g. via minor 'dry' mergers; Naab et al. 2009).

7.2 Post-starburst galaxies at $0.5 < z < 1$

At intermediate redshifts ($0.5 < z < 1$), our structural analyses reveal that PSBs have significantly different structures to their counterparts at $z > 1$. The main results from our structural analyses can be summarised as follows:

(i) PSBs at intermediate redshift ($0.5 < z < 1$) are generally of low mass ($M_* < 10^{10}\,M_\odot$), and exhibit structures that are still relatively compact [$r_e \sim 0.2$ arcsec, (1.4 kpc)] but of much lower Sérsic index ($n \sim 1.7$) than the massive PSBs at $z > 1$. These PSBs are more compact than the general low-mass star-forming population, but have structures similar to those of low-mass passive galaxies (i.e. passive discs), the population into which they will most likely evolve. We note that more massive PSBs ($M_* > 10^{10}\,M_\odot$) do exist at this epoch, but these galaxies are rare and interestingly exhibit high n values similar to the massive PSBs at $z > 1$. This suggests that the quenching process producing massive PSBs at $z > 1$ still occurs at lower redshifts but at a much lower frequency (see Sections 4.1 and 4.3). Finally, we note that the presence of a known supercluster in the CANDELS–UDS field at this epoch ($z \sim 0.65$; van Breukelen et al. 2006; Galametz et al. 2018) appears to cause no significant bias in these results. Using the K-band structural parameters of Almaini et al. (2017), which were determined for all galaxies in our parent sample (i.e. the full UDS field; see Section 2.3), we find entirely consistent results for each galaxy population.

(ii) PSBs at this epoch do not show any evidence for significant point source emission. This suggests that neither an AGN, nor an unresolved decaying nuclear starburst are significant during the post-starburst phase. However, we cannot rule out that these events were related to the quenching of these galaxies (see Section 5.1).

(iii) Bulge–disc decomposition indicates that PSBs at this epoch contain a significant disc component ($B/T < 0.4$), which has survived the event that quenched the star-formation. Their B/T is similar to those of the low-mass passive population (see Section 5.2). This result is consistent with previous works at this epoch, which find that although PSBs are a morphologically heterogeneous population, they generally exhibit disc-like morphologies (e.g. Dressler et al. 1999; Caldwell et al. 1999; Tran et al. 2003; Poggianti et al. 2009; Vergani et al. 2010; Pawlik et al. 2016).

(iv) PSBs at $0.5 < z < 1$ exhibit consistent structural parameters (r_e, n) between all four wavebands studied at this epoch. This similarity between wavebands probing both the old stellar component ($\lambda_{rest} > 4000$ Å; I_{F814W}, J_{F125W} and H_{F160W}) and younger stellar populations (O B A F stars; $\lambda_{rest} < 4000$ Å; V_{F606W}) indicates that younger stars are tracing the old stellar population (i.e. stellar mass) in these galaxies. As with PSBs at $z > 1$, this suggests that any preceding starburst, extended star-formation episode and/or quenching was not strongly centralized, and occurred throughout the stellar distribution (i.e. globally; see Section 6).

Taken together, these results suggest that intermediate-z PSBs ($0.5 < z < 1$) have not experienced a major disruption to their stellar distribution (e.g. major merger or disc collapse), and that consequently the quenching mechanism responsible must be a relatively gentle process. We note that although PSBs at this epoch are generally more compact than analogous star-forming galaxies (i.e. those of similar mass), this does not necessarily imply that these galaxies have experienced a violent 'compaction' event. In fact the low Sérsic indices of this population would suggest that this is not the case. With respect to major mergers, we also note that while a new disc may eventually reform, the timescale involved is expected to be longer than that of the PSB phase (> 1 Gyr, see e.g. Athanassoula et al. 2016). Consequently, these events are unlikely to be the origin of the disc-dominated PSBs at this epoch. Furthermore, given that at this epoch not all star-forming galaxies are expected to experience a PSB phase (e.g. Wild et al. 2016; Socolovsky et al. 2018), the general star-forming population may not be representative of the true progenitors of these PSBs. We explore this issue in more detail in a forthcoming publication (Socolovsky et al., in preparation). Finally, we note that since these intermediate-z PSBs have structures very similar to low-mass passive galaxies (i.e. passive discs), it is likely that any significant structural changes related to the quenching process have already taken place, and that these galaxies are simply quietly transitioning into established passive discs (i.e. S0s). The resultant fading of the stellar disc leading to the slight increase in n and B/T observed (see Fig. 12).

In comparison to previous works, we note that gas-rich major mergers have been linked to PSBs at $0.5 < z < 1$ (e.g. Wild et al. 2009; Wu et al. 2014), which is in apparent contrast to our findings. However, these previous studies focus on massive PSBs ($M* > 10^{10}\,M_\odot$), which are rare in the CANDELS–UDS field at this epoch (see Fig. 1). Consequently, our findings are not in contradiction to these previous works, but suggest an alternative, less disruptive process is primarily responsible for PSBs at lower masses ($M_* < 10^{10}\,M_\odot$). Furthermore, we note that at this epoch, the rare, massive PSBs in the CANDELS–UDS field do exhibit the high Sérsic indices expected for the remnant of a gas-rich major merger, which is consistent with these previous studies.

With respect to the dominant quenching mechanism, our results suggest two scenarios for PSBs at this epoch: i) these galaxies experience a weaker disruptive event to the PSBs at $z > 1$ which allowed their disc-dominated structures to survive, e.g. minor mergers; or ii) they are a sub-population of disc galaxies that have experienced gas stripping/removal (e.g. via AGN/stellar feedback or environmental processes) and a subsequent disc fading. Since the PSBs at this epoch are typically of low mass ($M_* < 10^{10}\,M_\odot$), such processes would have a strong potential to cause the rapid quenching of star formation, necessary to produce the characteristic PSB spectral features (i.e. strong Balmer absorption), without significant structural influence. Disentangling these quenching scenarios is beyond the scope of this work, but the role of environment in quenching PSBs at $0.5 < z < 1$ is explored in detail by the recent study of Socolovsky et al. (2018), which also uses the PSBs identified from the full UDS field. Furthermore, we note that the lack of excess intermediate–young aged stars (O B A F) in the central regions of these PSBs might place useful constraints on the quenching process, as it suggests the resultant star-burst was either very weak, or global in nature. We shall explore this issue in future work. Finally, with respect to the potential quenching processes, we note that recent gas measurements for both local PSBs ($z \lesssim 0.1$; French et al. 2015; Rowlands et al. 2015) and two PSBs at higher redshift ($z \sim 0.7$; Suess et al. 2017) suggest that the complete removal or depletion of the molecular gas reservoir is not necessarily

required to terminate star-formation. We also explore this issue, and the cold interstellar medium (ISM) content of PSBs in the full UDS field across a wide redshift range ($0.5 < z < 2$), in a forthcoming publication (Rowlands et al., in preparation).

8 CONCLUSIONS

In this study, we present a detailed analysis of the structure of PSBs at $0.5 < z < 2$ using data from the UDS and CANDELS. Using a large sample of photometrically-selected PSBs recently identified in the UDS field (Wild et al. 2016), we examine the structure of ~ 80 of these recently-quenched systems, and compare to a large sample of ~ 2000 passive and star-forming galaxies. For our analysis we use a combination of near-infrared and optical $\mu(r)$ profiles, obtained from CANDELS *HST* imaging, which probe both the old stellar component as well as younger, and more recently formed stellar populations (i.e. O B A F stars). Using both stacked and individual $\mu(r)$ profiles, various structural analyses have been performed, including single Sérsic and multiple component fits, which have revealed significant differences in the structure of PSBs at different epochs.

At high redshift ($1 < z < 2$), PSBs are typically massive ($M_* > 10^{10}\,M_\odot$), ultra compact, bulge-dominated and have high Sérsic indices. In general, the structure of these PSBs differs significantly from their star-forming progenitors and is very similar to those of the old massive passive population, but considerably more compact. These results indicate that these galaxies were quenched in a relatively violent event (e.g. gas-rich major merger or dissipative 'protogalactic' collapse) that produced a very compact, centrally-condensed remnant. Furthermore, we also find consistent structures for these PSBs across all the wavebands studied ($I_{\rm F814W}$, $J_{\rm F125W}$ and $H_{\rm F160W}$), regardless of whether the old stellar component or younger (O B A F) stellar populations are being principally traced. Our results suggest that for most PSBs at this epoch, any preceding starburst and/or quenching was not strongly centralised and occurred throughout the stellar distribution (i.e. it was global in nature).

In contrast, at lower redshifts ($0.5 < z < 1$), the structure of PSBs is significantly different. At this epoch, PSBs are generally of low mass ($M_* < 10^{10}\,M_\odot$), and exhibit structures that are still relatively compact, but disc-dominated and of much lower Sérsic index than PSBs at $z > 1$. Their structures are similar to the low-mass passive population (i.e. passive discs), the population into which they will most likely evolve. These results suggest that these galaxies have been quenched by a more gentle process that did not significantly disrupt the stellar distribution, and allowed their disc structures to survive (e.g. environmental processes such as gas stripping and/or minor mergers). Furthermore, we also find consistent structures for these PSBs in all the wavebands studied ($V_{\rm F606W}$, $I_{\rm F814W}$, $J_{\rm F125W}$ and $H_{\rm F160W}$), regardless of whether the old stellar component or younger (O B A F) stellar populations are being principally traced. Consequently, as with PSBs at $z > 1$, our results suggest that any preceding starburst and/or quenching was not strongly centralized and occurred throughout the stellar distribution (i.e. globally).

In conclusion, we find that PSBs (i.e. recently-quenched galaxies) at $z > 1$ are an intrinsically different population to those at lower redshifts. Our results indicate that different quenching routes are active at different epochs, with the PSB phase being triggered by different evolutionary processes.

9 ACKNOWLEDGEMENTS

This work is based on observations taken by the CANDELS Multi-Cycle Treasury Program with the NASA/ESA HST, which is operated by the Association of Universities for Research in Astronomy, Inc., under NASA contract NAS5-26555. DTM acknowledges support from STFC. NAH acknowledges support from STFC through an Ernest Rutherford Fellowship.

REFERENCES

Almaini O., et al., 2017, MNRAS, 472, 1401
Athanassoula E., Rodionov S. A., Peschken N., Lambert J. C., 2016, ApJ, 821, 90
Bell E. F., et al., 2004, ApJ, 608, 752
Belli S., Newman A. B., Ellis R. S., 2015, ApJ, 799, 206
Bertin E., Arnouts S., 1996, A&AS, 117, 393
Best P. N., Kauffmann G., Heckman T. M., Brinchmann J., Charlot S., Ivezić Ž., White S. D. M., 2005, MNRAS, 362, 25
Best P. N., Kaiser C. R., Heckman T. M., Kauffmann G., 2006, MNRAS, 368, L67
Bezanson R., van Dokkum P., van de Sande J., Franx M., Kriek M., 2013, ApJ, 764, L8
Blake C., et al., 2004, MNRAS, 355, 713
Brammer G. B., et al., 2011, ApJ, 739, 24
Bruce V. A., et al., 2014, MNRAS, 444, 1660
Bruzual G., Charlot S., 2003, MNRAS, 344, 1000
Buitrago F., Trujillo I., Conselice C. J., Häußler B., 2013, MNRAS, 428, 1460
Caldwell N., Rose J. A., Dendy K., 1999, AJ, 117, 140
Carollo C. M., et al., 2013, ApJ, 773, 112
Chabrier G., 2003, PASP, 115, 763
Charlot S., Fall S. M., 2000, ApJ, 539, 718
Cirasuolo M., et al., 2007, MNRAS, 380, 585
Dekel A., Birnboim Y., 2006, MNRAS, 368, 2
Dekel A., et al., 2009, Nature, 457, 451
Diamond-Stanic A. M., Moustakas J., Tremonti C. A., Coil A. L., Hickox R. C., Robaina A. R., Rudnick G. H., Sell P. H., 2012, ApJ, 755, L26
Dressler A., Gunn J. E., 1983, ApJ, 270, 7
Dressler A., Smail I., Poggianti B. M., Butcher H., Couch W. J., Ellis R. S., Oemler Jr. A., 1999, ApJS, 122, 51
Faber S. M., et al., 2007, ApJ, 665, 265
Fisher D. B., Drory N., 2011, ApJ, 733, L47
French K. D., Yang Y., Zabludoff A., Narayanan D., Shirley Y., Walter F., Smith J.-D., Tremonti C. A., 2015, ApJ, 801, 1
Furusawa H., et al., 2008, ApJS, 176, 1
Galametz A., et al., 2018, MNRAS, 475, 4148
Goto T., 2007, MNRAS, 381, 187
Grogin N. A., et al., 2011, ApJS, 197, 35
Gunn J. E., Gott III J. R., 1972, ApJ, 176, 1
Hartley W. G., et al., 2013, MNRAS, 431, 3045
Hopkins P. F., 2012, MNRAS, 420, L8
Hopkins P. F., Hernquist L., Cox T. J., Di Matteo T., Martini P., Robertson B., Springel V., 2005, ApJ, 630, 705
Hopkins P. F., Cox T. J., Younger J. D., Hernquist L., 2009, ApJ, 691, 1168
Jedrzejewski R. I., 1987, MNRAS, 226, 747
Keating S. K., Abraham R. G., Schiavon R., Graves G., Damjanov I., Yan R., Newman J., Simard L., 2015, ApJ, 798, 26
Koekemoer A. M., et al., 2011, ApJS, 197, 36
Kron R. G., 1980, ApJS, 43, 305
Lani C., et al., 2013, MNRAS, 435, 207
Larson R. B., Tinsley B. M., Caldwell C. N., 1980, ApJ, 237, 692
Lawrence A., et al., 2007, MNRAS, 379, 1599
MacArthur L. A., Courteau S., Holtzman J. A., 2003, ApJ, 582, 689
Maltby D. T., et al., 2012a, MNRAS, 419, 669
Maltby D. T., Hoyos C., Gray M. E., Aragón-Salamanca A., Wolf C., 2012b, MNRAS, 420, 2475

Maltby D. T., Aragón-Salamanca A., Gray M. E., Hoyos C., Wolf C., Jogee S., Böhm A., 2015, MNRAS, 447, 1506
Maltby D. T., et al., 2016, MNRAS, 459, L114
Martig M., Bournaud F., Teyssier R., Dekel A., 2009, ApJ, 707, 250
McDonald M., Courteau S., Tully R. B., Roediger J., 2011, MNRAS, 414, 2055
Mortlock A., et al., 2013, MNRAS, 433, 1185
Muzzin A., et al., 2013, ApJ, 777, 18
Naab T., Johansson P. H., Ostriker J. P., 2009, ApJ, 699, L178
Newman A. B., Belli S., Ellis R. S., 2015, ApJ, 813, L7
Norton S. A., Gebhardt K., Zabludoff A. I., Zaritsky D., 2001, ApJ, 557, 150
Pawlik M. M., Wild V., Walcher C. J., Johansson P. H., Villforth C., Rowlands K., Mendez-Abreu J., Hewlett T., 2016, MNRAS, 456, 3032
Pawlik M. M., et al., 2018, MNRAS, 477, 1708
Peng C. Y., Ho L. C., Impey C. D., Rix H.-W., 2002, AJ, 124, 266
Poggianti B. M., et al., 2009, ApJ, 693, 112
Pozzetti L., et al., 2010, A&A, 523, A13
Pracy M. B., et al., 2013, MNRAS, 432, 3131
Rowlands K., Wild V., Nesvadba N., Sibthorpe B., Mortier A., Lehnert M., da Cunha E., 2015, MNRAS, 448, 258
Shen S., Mo H. J., White S. D. M., Blanton M. R., Kauffmann G., Voges W., Brinkmann J., Csabai I., 2003, MNRAS, 343, 978
Silk J., Rees M. J., 1998, A&A, 331, L1
Simpson C., et al., 2012, MNRAS, 421, 3060
Simpson C., Westoby P., Arumugam V., Ivison R., Hartley W., Almaini O., 2013, MNRAS, 433, 2647
Socolovsky M., Almaini O., Hatch N. A., Wild V., Maltby D. T., Hartley W. G., Simpson C., 2018, MNRAS, 476, 1242
Strateva I., et al., 2001, AJ, 122, 1861
Suess K. A., Bezanson R., Spilker J. S., Kriek M., Greene J. E., Feldmann R., Hunt Q., Narayanan D., 2017, ApJ, 846, L14
Szomoru D., et al., 2010, ApJ, 714, L244
Szomoru D., Franx M., van Dokkum P. G., 2012, ApJ, 749, 121
Tacchella S., Dekel A., Carollo C. M., Ceverino D., DeGraf C., Lapiner S., Mandelker N., Primack J. R., 2016, MNRAS, 458, 242
Tran K.-V. H., Franx M., Illingworth G., Kelson D. D., van Dokkum P., 2003, ApJ, 599, 865
Trujillo I., et al., 2006, MNRAS, 373, L36
Vergani D., et al., 2010, A&A, 509, A42
Wellons S., et al., 2015, MNRAS, 449, 361
Whitaker K. E., Kriek M., van Dokkum P. G., Bezanson R., Brammer G., Franx M., Labbé I., 2012, ApJ, 745, 179
Whitaker K. E., et al., 2013, ApJ, 770, L39
Wild V., Walcher C. J., Johansson P. H., Tresse L., Charlot S., Pollo A., Le Fèvre O., de Ravel L., 2009, MNRAS, 395, 144
Wild V., et al., 2011, MNRAS, 410, 1593
Wild V., et al., 2014, MNRAS, 440, 1880
Wild V., Almaini O., Dunlop J., Simpson C., Rowlands K., Bowler R., Maltby D., McLure R., 2016, MNRAS, 463, 832
Williams R. J., Quadri R. F., Franx M., van Dokkum P., Toft S., Kriek M., Labbé I., 2010, ApJ, 713, 738
Williams C. C., et al., 2017, ApJ, 838, 94
Wu P.-F., Gal R. R., Lemaux B. C., Kocevski D. D., Lubin L. M., Rumbaugh N., Squires G. K., 2014, ApJ, 792, 16
Yamauchi C., Goto T., 2005, MNRAS, 359, 1557
Yano M., Kriek M., van der Wel A., Whitaker K. E., 2016, ApJ, 817, L21
Zabludoff A. I., Zaritsky D., Lin H., Tucker D., Hashimoto Y., Shectman S. A., Oemler A., Kirshner R. P., 1996, ApJ, 466, 104
Zolotov A., et al., 2015, MNRAS, 450, 2327
de Jong R. S., 1996, A&AS, 118, 557
de Vaucouleurs G., 1959, Handbuch der Physik, 53, 311
van Breukelen C., et al., 2006, MNRAS, 373, L26
van de Sande J., et al., 2013, ApJ, 771, 85
van der Wel A., et al., 2011, ApJ, 730, 38
van der Wel A., et al., 2012, ApJS, 203, 24
van der Wel A., et al., 2014, ApJ, 788, 28

This paper has been typeset from a TEX/LATEX file prepared by the author.